Bioorg. Med. Chem. 110 (2024) 117829

Contents lists available at ScienceDirect

Bioorganic & Medicinal Chemistry

journal homepage: www.elsevier.com/locate/bmc

Chiral pyrrolidines as multipotent agents in Alzheimer and neurodegenerative diseases

Antonio Carrieri [a,*], Alexia Barbarossa [a], Modesto de Candia [a], Francesco Samarelli [a], Cosimo Damiano Altomare [a], Kinga Czarnota-Łydka [b], Sylwia Sudoł-Tałaj [b], Gniewomir Latacz [b], Jadwiga Handzlik [b], Leonardo Brunetti [a], Luca Piemontese [a], Francesco Limongelli [a], Giovanni Lentini [a], Alessia Carocci [a,*]

[a] Dipartimento di Farmacia-Scienze del Farmaco, Università degli Studi di Bari, Via Orabona, 4, 70125 Bari, Italy
[b] Department of Technology and Biotechnology of Drugs, Faculty of Pharmacy, Jagiellonian University, Medical College, Medyczna 9, PL 30-688 Kraków, Poland

ARTICLE INFO

Keywords:
Alzheimer's disease
Neurodegeneration
Antioxidants
Multi-functional drugs
Donepezil
FAAH
Acetylcholinesterase
Butyrylcholinesterase

ABSTRACT

In pharmaceutical science and drug design the versatility of the pyrrolidine scaffold relating to spatial arrangement, synthetic accessibility and pharmacological profile is a largely explored and most likely interesting one. Nonetheless, few evidences suggest the pivotal role of pyrrolidine as scaffold for multipotent agents in neurodegenerative diseases. We then challenged the enrolling in the field of Alzheimer disease of so far not ravelled targets of this chemical cliché with a structure based and computer-aided design strategy focusing on multi-target action, versatile synthesis as well as pharmacological safeness. To achieve these hits, ten enantiomeric pairs of compounds were obtained and tested, and the biological data will be here presented and discussed. Among the novel compounds, coumarin and sesamol scaffolds containing analogues resulted promising perspectives.

1. Introduction

More than half of all the unique small-molecule drugs approved by the Food and Drug Administration (FDA) contains nitrogen, with nitrogenated heterocyclic compounds accounting for almost two-thirds of the total amount. Flat heteroaromatic (pyridine, imidazole, indole, tetrazole, and thiazole) or non-flat saturated ring systems (piperidine, piperazine, and pyrrolidine) are the most popular, with many pyrrolidines being substituted at the nitrogen atom. Within these instances, the pyrrolidine moiety is widely present in natural products, especially in alkaloids isolated from plants or microorganisms, endowing them with different biological activities. Examples include nicotine (antioxidant, anti-inflammatory, and antihyperglycemic properties), scalusamides A and (*R*)-bugaine (antimicrobial and antifungal properties), 1,4-dideoxy-1,4-imino-d-ribitol, and aegyptolidine A (anticancer properties). The interest in this saturated scaffold is enhanced by the possibility of efficiently exploring the pharmacophore space due to sp^3-hybridization, input to the molecules stereochemistry, and the increased three-dimensional coverage due to the non-planarity of the ring system, the so called pseudorotation.[1] Therefore, it is not surprising that the pyrrolidine nucleus is among the preferred scaffolds in pharmaceutical sciences and drug design, as evidenced by the fact that it ranks first among the top five most common five-membered non-aromatic nitrogen heterocycles, appearing in thirty-seven new molecular and/or first in class entities approved by the FDA, including captopril, lincomycin, clemastin, and remoxipride.[2] In the last few decades, several novel derivatives of pyrrolidine have been synthesized for their CNS potential and proved to be effective in the treatment of psychiatric illness and other CNS disorders.[3] Different *N*-(pyrrolidin-3-yl)-naphthamide analogs bind with high affinity for both the D_2 and D_3 dopamine receptor subtypes,[4] and several pyrrolidine derivatives have been designed as conformationally restricted analogs of profadol for analgesic activity. Beside these, several pyrrolidine-containing compounds aimed at treating Alzheimer's disease (AD) have been proposed over time (i.e., pyrrolidine derived as β-secretase-1 inhibitors).[5] AD is a progressive neurodegenerative disorder associated with the appearance of extracellular senile or neuritic plaques and intracellular neurofibrillary tangles in the brain, which induce memory loss and cognitive impairment, causing enormous suffering to individuals, families, and society. AD is now deemed by the World Health Organization as the most common

* Corresponding authors.
E-mail addresses: antonio.carrieri@uniba.it (A. Carrieri), alessia.carocci@uniba.it (A. Carocci).

https://doi.org/10.1016/j.bmc.2024.117829
Received 22 April 2024; Received in revised form 24 June 2024; Accepted 1 July 2024
Available online 3 July 2024

cause of dementia, counting approximately 50 million patients worldwide, and it is estimated that it will affect 75 million people by 2030 and 140 million people by 2050 globally.[6] The complex multifactorial pathogenesis of AD makes it difficult to develop new drugs and leads to the failure of many promising drug candidates in clinical trials. Therefore, research on AD is still a hot topic, and the efforts and attempts of scientific groups worldwide are continuing with the aim of finding an effective treatment. The current understanding of AD has led to the identification of primary targets that influence the generation and exacerbation of the disease, including enzymes acetylcholinesterase (AChE) and butyrylcholinesterase (BChE), β-secretase-1 (BACE-1), aggregation of Aβ (β-amyloid), monoamine oxidases (MAOs) and NMDA receptors. More recently, neuroinflammation has also emerged as an important factor in AD pathology, and as a result, researchers have turned to the endocannabinoid system as a source for novel therapeutics. Particularly, the inhibition of fatty acid amide hydrolase (FAAH), the main catabolic enzyme degrading endocannabinoid anandamide, has been the object of significant attention due to its capability to enhance the endocannabinoid tone without inducing significant psychoactive effects.[7] Linked to neuroinflammation, oxidative stress is also an important factor in the progression of this disorder because it can trigger many pathological cascades.[8] These targets have served as an objective for the development of numerous bioactive compounds, several of which have been proposed for the treatment of AD, nonetheless, only four drugs have currently been approved for clinical use by the FDA: three AChE inhibitors (donepezil, galantamine, and rivastigmine, Fig. 1) and an NMDA receptor antagonist, memantine. All of them are single-target drugs that can significantly improve the condition of patients with cognitive deterioration and memory loss, however, they are unable to halt disease progression. In view of the complex pathogenesis of AD, research on multi-target therapeutic agents, meaning pharmaceuticals targeting more than one etiopathological factor, has become increasingly popular. Such compounds could exert synergistic effects on the whole network of pathological targets, leading to improved memory and cognition and, possibly, even altering the clinical course of the disease.[9] In this intriguing scenario, this study is focused on design and synthesis of *N*-substituted pyrrolidine derivatives as neuroprotective multi-target agents for potential treatment of AD. This project effort was stimulated by the evidence that the highly versatile and intriguing pyrrolidine ring has not been fully explored in cholinesterases and FAAH inhibitor scaffolds, as well as in those of valuable antioxidant agents. In addition, these compounds might be interesting because of their potential stereoselective activities: the probability of clinical exploitation of newly developed drugs has been related to the fraction of sp^3 hybridized carbon atoms (Fsp^3) and the number of chirality centers.[10] Thus, a recently designed and synthesized series of *N*-substituted aryloxymethyl pyrrolidines (Fig. 1) in their enantiopure forms, initially investigated to assess stereochemical requirements of the ligand-binding site of P-gp, was considered.[11]

We explored the anti-AD potential of these compounds by first studying their activity as AChE inhibitors thanks to a certain degree of similarity with the pharmacophoric elements of the well-known AChE inhibitor donepezil (i.e. chargeable nitrogen with a lipophilic pendant, stereocenter, hydrogen bond accepting atom, and aromatic rings), that could endow our ligands with a similar pharmacological profile, and that was also confirmed by three-dimensional similarity and shape-matching fit of the chiral pyrrolidines to the donepezil bioactive conformation (see infra). This hint prompted us to synthesize a series of novel enantiomeric couples and test their activities against the aforementioned targets. The achieved results are described in this manuscript.

2. Results and discussion

2.1. Chemistry

N-Substituted 2-aryloxymethylpyrrolidines (**5a**–**7a**, **8b**, **9c**, **10d**, **11**–**12e**, **13f**, **14g**) were prepared in their enantiopure form, according to a synthetic route previously reported and described in Scheme 1.[11] Firstly, the amino groups of the commercial enantiopure pyrrolidin-2-ylmethanols (*R*)- and (*S*)-**1** were Boc-protected as previously described. The obtained *N*-Boc amino alcohols (*R*)- and (*S*)-**2** were reacted with the suitable aryl alcohol according to the Mitsunobu procedure[12] to give the corresponding aryl alkyl ethers (*R*)- and (*S*)-**3a–g**. The removal of the Boc protecting group with trifluoroacetic acid[13] afforded the aryloxy methyl pyrrolidines (*R*)- and (*S*)-**4a–g**, which were

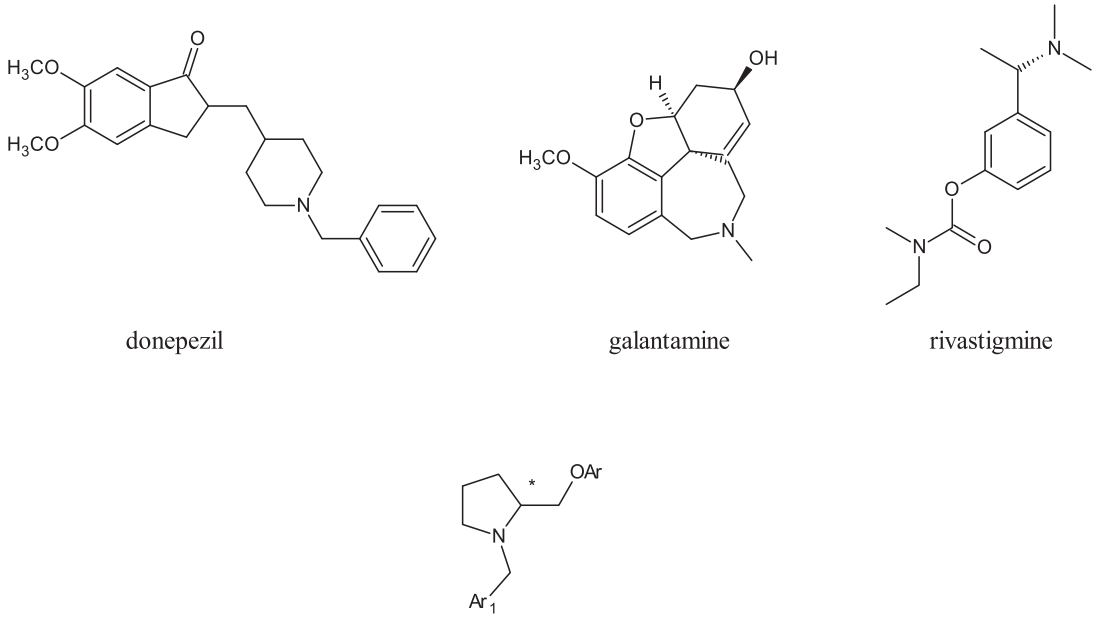

Fig. 1. FDA approved AChE inhibitors structures and general structure for chiral *N*-substituted aryloxymethyl pyrrolidines.

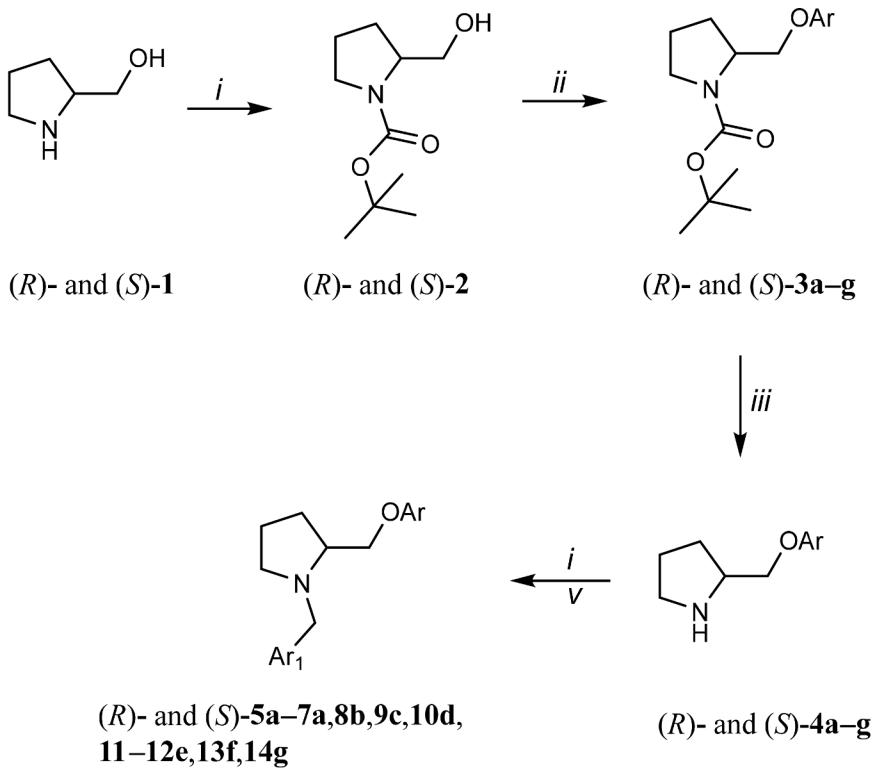

a: Ar = 1,3-benzodioxole-5-yl
b: Ar = 3-methoxyphenyl
c: Ar = 3,4-dimethoxyphenyl
d: Ar = 2,3-dichlorophenyl
e: Ar = 3-nitrophenyl
f: Ar = 2-oxo-2*H*-chromen-7-yl
g: Ar = 2-oxo-4-phenyl-2*H*-chromen-7-yl

5,**11**: Ar_1 = phenyl
6: Ar_1 = 2-fluorophenyl
7–10,**12–14**: Ar_1 = naphthalen-1-yl

Scheme 1. *Reagents and conditions*: i) Boc_2O, NaOH, THF, rt; ii) suitable ArOH, TPP, DIAD, anhyd·THF, rt; iii) CF_3COOH, CH_2Cl_2, rt, 12 h; iv) suitable bromide, Et_3N, abs EtOH, rt, 24 h.

then converted into the final *N*-substituted aryloxy methyl pyrrolidines with the appropriate bromide. 1-(Bromomethyl)naphthalene (**16**), used for the synthesis of the final compounds **7a**, **8b**, **9c**, **10d**, **13f**, and **14g** has been synthesized starting from 1-(hydroxymethyl)naphthalene (**15**) as depicted in Scheme 2.

2.2. Biological results

2.2.1. AChE and BChE inhibition activity

The in vitro activity of all presented enantiomer pairs was measured toward electric eel (*ee*) AChE, and horse serum (*hs*) BChE, by applying the Ellman colorimetric assay, with slight modifications.[14–16] All

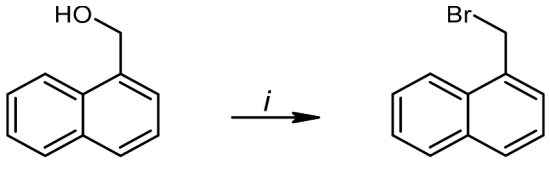

Scheme 2. *Reagents and conditions*: i) PBr_3, 0 °C, 2 h → rt, 24 h.

derivatives were first tested at a single point 10 μM concentration, and those showing at least 35 % inhibition were further tested to determine their half-maximal inhibitory concentrations (IC_{50} values). Donepezil and tacrine were tested as positive controls against AChE and BChE, respectively. The results (Table 1) suggested that substituent fragments on pyrrolidine ring, as well as stereoisomerism, deeply affected the activity profile.

Most of the *R*-enantiomers achieved a low-to-moderate inhibition over *ee*AChE and a weak activity against *eq*BChE, except for derivative (*R*)-**7a**, which returned as the most interesting *ee*AChE inhibitor, thus showing activity in the submicromolar range (IC_{50} = 0.215 μM). A better inhibition of BChE was achieved by most of the *S*-enantiomers that also reported a weak AChE inhibition. The most active *S*-enantiomer as BChE inhibitor was compound (*S*)-**14g** (IC_{50} = 0.155 μM). Both enantiomers of the 3-nitrophenoxy ethers (compounds **11e** and **12e**) appeared as selective inhibitors of AChE. The *N*-benzyl derivative (*R*)-**11e** (IC_{50} = 1.3 μM) was six times more active than the corresponding *S*-isomer. Whilst the replacement of the phenyl ring by a naphthyl reversed the pattern of stereoselectivity, thus showing derivative (*S*)-**12e** a significant higher activity than (*R*)-**12e**, and it was only two times less active than (*R*)-**11e**. Curiously, a similar reversal of stereoselectivity depending on the size and substituents of the aryl rings was previously reported for pyrrolidinomethyl aryl ethers acting as P-glycoprotein (P-gp) modulators[11] or

Table 1
Biological activity of compounds under study [(*R*)- and (*S*)-**5a**–**7a**,**8b**,**9c**,**10d**,**11e**,**12e**,**13f**,**14g**] towards *ee*AChE and *hs*BChE, *h*FAAH enzymes and antioxidant potencies in the DCFH-DA assay towards HepG2 and SHSY-5Y cell lines.

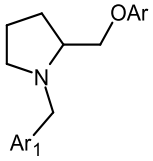

Ar	Ar$_1$	compd	***ee*AChE**[a] IC_{50}, μM[c] (or % inhib)[d]	***eq*BChE**[b] IC_{50}, μM[c] (or % inhib)[d]	***h*FAAH**[e] IC_{50}, μM[f]	**DCFDH-DA** IC_{50}, μM[f]	
						HepG2	**SH-SY5Y**
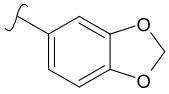	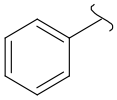	(*R*)-**5a**	3.15 ± 0.27	2.2 ± 0.5	22.0 ± 4.0	19.7 ± 0.5	>100
		(*S*)-**5a**	(38 ± 3)	0.656 ± 0.130	19.0 ± 5.0	78.3 ± 0.6	>100
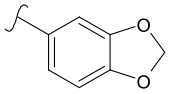	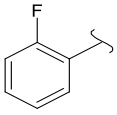	(*R*)-**6a**	0.950 ± 0.110	(25 ± 6)	16.1 ± 1.2	>100	62.4 ± 1.0
		(*S*)-**6a**	(32 ± 2)	9.91 ± 0.15	9.6 ± 0.5	85.7 ± 0.2	1.8 ± 0.5
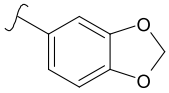	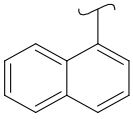	(*R*)-**7a**	0.215 ± 0.005	(27 ± 6)	8.2 ± 1.9	0.4 ± 0.5	8.4 ± 0.2
		(*S*)-**7a**	(32 ± 1)	(7 ± 4)	23.4 ± 4.2	62.3 ± 0.2	31.2 ± 1.0
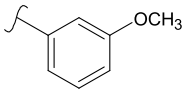	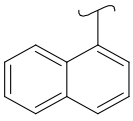	(*R*)-**8b**	10.3 ± 2.1	2.03 ± 0.13	8.8 ± 1.3	>100	>100
		(*S*)-**8b**	15.7 ± 1.1	1.70 ± 0.11	7.3 ± 0.7	>100	>100
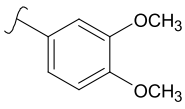	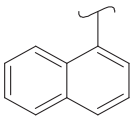	(*R*)-**9c**	10.0 ± 1.2	11.2 ± 0.5	1.8 ± 0.8	48.6 ± 2.0	>100
		(*S*)-**9c**	(20 ± 10)	(18 ± 11)	14.6 ± 1.5	>100	>100
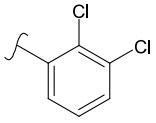	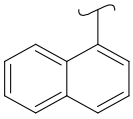	(*R*)-**10d**	(13 ± 4)	10.0 ± 0.24	9.8 ± 1.1	65.3 ± 1.0	>100
		(*S*)-**10d**	(17 ± 6)	2.8 ± 0.9	8.87 ± 0.14	>100	>100
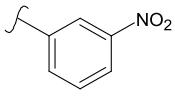	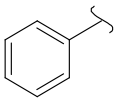	(*R*)-**11e**	1.31 ± 0.42	(18 ± 5)	8.8 ± 1.7	6.4 ± 0.5	>100
		(*S*)-**11e**	7.22 ± 0.25	(13 ± 2)	6.06 ± 0.26	>100	>100
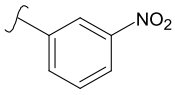	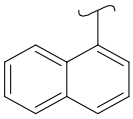	(*R*)-**12e**	16.7 ± 1.5	11.1 ± 0.6	5.3 ± 2.1	>100	>100
		(*S*)-**12e**	2.66 ± 0.21	(14.5 ± 0.3)	13.0 ± 3.0	35.3 ± 1.0	94.2 ± 1.0

(*continued on next page*)

Table 1 (*continued*)

Ar	Ar_1	compd	*ee*AChE[a] IC_{50}, μM[c] (or % inhib)[d]	*eq*BChE[b] IC_{50}, μM[c] (or % inhib)[d]	*h*FAAH[e] IC_{50}, μM[f]	DCFDH-DA IC_{50}, μM[f]	
						HepG2	SH-SY5Y
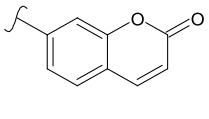	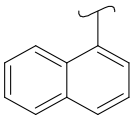	(*R*)-**13f**	3.73 ± 0.20	(35 ± 5)	1.1 ± 0.3	78.3 ± 2.0	86.5 ± 0.5
		(*S*)-**13f**	2.35 ± 0.11	0.950 ± 0.040	0.51 ± 0.07	>100	>100
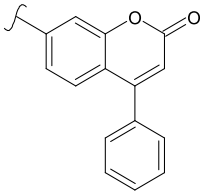	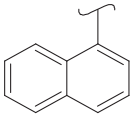	(*R*)-**14g**	19.0 ± 0.8	0.640 ± 0.260	2.1 ± 0.7	42.7 ± 1.4	55.4 ± 0.8
		(*S*)-**14g**	9.90 ± 1.05	0.155 ± 0.018	0.94 ± 0.06	86.4 ± 1.4	>100
		Donepezil	0.021 ± 0.011	2.25 ± 0.30	n.d.	n.d.	n.d.
		Tacrine	0.030 ± 0.010	0.020 ± 0.009	n.d.	n.d.	n.d.
		JZL195	n.d.	n.d.	0.019 ± 0.003	n.d.	n.d.
		Quercetin	n.d.	n.d.	n.d.	12.5 ± 0.4	5.6 ± 0.4

[a]Electric eel acetylcholinesterase. [b]Horse serum butyrylcholinesterase. [c]IC_{50} values by regression of the sigmoid dose–response curves through GraphPad Prism software (vers. 5.01). Data are means ± s.e.m. of three independent measurements. At least five-to-seven different concentrations of each compound were used to determine IC_{50} values. [d]Inhibition percentage at 10 μM. Data are means ± s.e.m. of three independent measurements. Donepezil and tacrine were used as positive controls against acetylcholinesterases, and butyrylcholinesterase, respectively. Values obtained under the used experimental conditions. [e]human recombinant FAAH. [f]Values are the mean of at least three determinations performed in triplicate. n.d. = not determined.

5-$HT_{1B/1D}$ ligands.[17] By focusing on the sesamol fragment containing ethers **5a**–**7a**, the *R*-stereoisomers were found promising inhibitors of AChE, unlike their *S*-congeners. The activity profile of **5a**–**7a** was deeply affected by the lipophilicity of substituents on the pyrrolidine nitrogen, expressed as Log *D* values at the pH of assay conditions, by following the ranking Bn < 2-F-Bn < naphthylmethyl. The 2-F-benzyl derivative (*R*)-**6a** was three times more active than the unsubstituted congener (*R*)-**5a**. Most of all, the introduction of a naphthalene moiety achieved a significant increase of anti-AChE activity, being (*R*)-**7a** the most active AChE inhibitor of the series. Only both *R*- and *S*-enatiomers of the *N*-benzyl derivative **5a** also showed a moderate BChE inhibition, thus identifying them as dual acting inhibitors of cholinesterases. Compound (*S*)-**5a** showed a BChE inhibition two times higher than (*R*)-**5a**.

The methoxy derivatives **8b** and **9c**, designed as open analogues of the sesamol-containing derivatives, were found to be significantly less active than (*R*)-**7a** in the inhibition of AChE. Both enantiomers of compound **8b** showed a moderate BChE inhibition, without any significant difference between (*R*)-**8b** (IC_{50} = 2.03 μM) and (*S*)-**8b** (IC_{50} = 1.70 μM). The introduction of a second methoxy substituent in **9c** made a relevant lower BChE inhibition. Surprisingly, compounds (*R*)-**13f** and (*S*)-**13f** obtained by maintaining the naphthylmethyl substituent on pyrrolidine and substituting sesamol by a coumarin fragment, proved both a quite similar moderate anti-AChE potency. The enantiomer (*S*)-**13f** also showed BChE inhibition in the submicromolar range of concentration.

AChE and BChE share about 70 % sequence homology. The active site of both enzymes is a deep and narrow gorge, containing the high conserved catalytic triad, the so-called oxyanion hole stabilizing the transient tetrahedral enzyme-substrate complex, the acyl binding pocket (ABP), and the choline binding site at the bottom of the gorge. Finally, the peripheral active site (PAS) is located on the rim of the active site gorge. Two aromatic residues in the ABP, and six of the aromatic residues lining the AChE gorge rim and PAS of AChE are replaced by aliphatic residues in BChE, thus resulting the BChE cavity larger than AChE gorge, and able to recognize hindered groups.[18] On this basis, it can be explained that employing a 4-phenyl substituted coumarin group in compounds **14g** the most interesting inhibitors of BChE in the series were obtained. Furthermore, the stereochemistry significantly affected the activity profile, by showing the enantiomer (*S*)-**14g** (IC_{50} = 0.155 μM) a BChE inhibition four times higher than the corresponding (*R*)-**14g** (IC_{50} = 0.64 μM) isomer.

The inhibition mechanism of the most interesting compounds (*R*)-**7a**

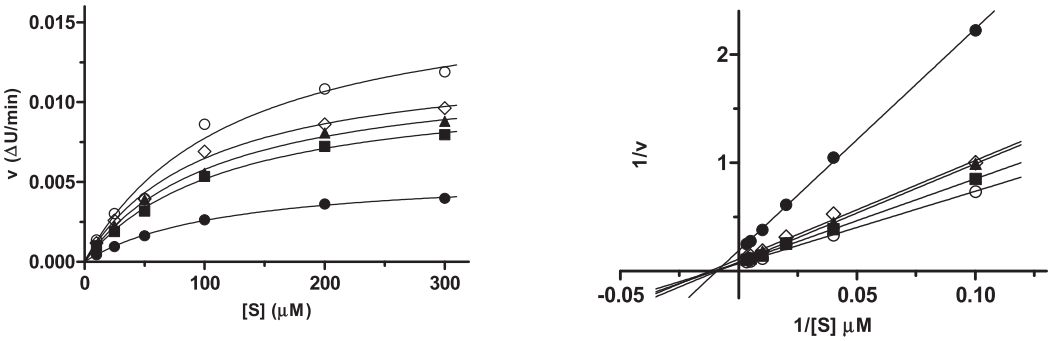

Fig. 2. Inhibition kinetics (letf) and Lineweaver–Burk plot (right), r^2 = 0.989–0.993 for *ee*AChE (0.18 U/mL) and (*R*)-**7a**, by using different substrate (acetylthiocholine iodide) concentrations (50–300 μM). (○) no inhibitor, (●) 10 μM, (■) 1 μM, (▲) 0.5 μM, (◇) 0.1 μM.

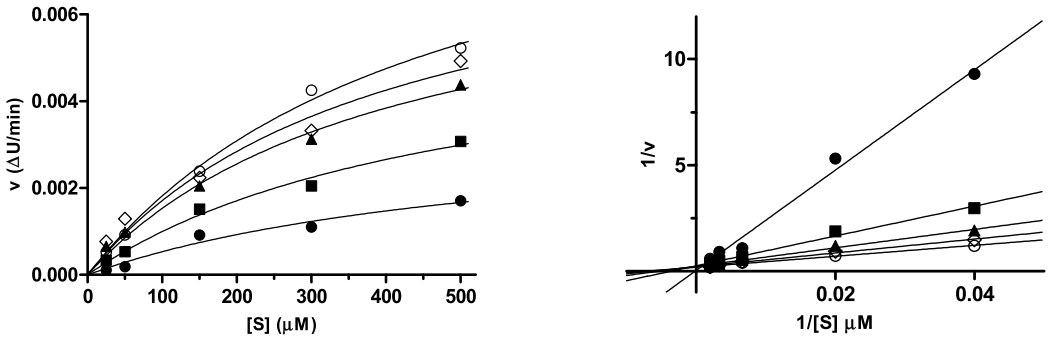

Fig. 3. Inhibition kinetics (letf) and Lineweaver–Burk plot (right), r^2 = 0.989–0.993 for *ee*BChE (0.18 U/mL) and (*S*)-**14g**, by using different substrate (acetylthiocholine iodide) concentrations (50–300 μM). (○) no inhibitor, (●) 1 μM, (■) 0.3 μM, (▲) 0.1 μM, (◇) 0.01 μM.

against AChE (Fig. 2), and (*S*)-**14g** against BChE (Fig. 3), respectively, was further studied. The Lineweaver-Burk curves were derived by varying the substrates concentrations (ranging from 25 to 300 μM for AChE, and from 25 to 500 μM for BChE), in the absence or presence of inhibitor at different concentrations. The study of binding of (*R*)-**7a**, to AChE changed both V_{max} and K_m values, as a trend that is generally ascribed to mixed-type inhibition (Fig. 2). A replot of the slopes versus the corresponding inhibitor concentrations provided a K_i value of 1.59 μM.

Compound (*S*)-**14g** also showed a mixed inhibition of *eq*BChE, and replot of the slopes versus the corresponding inhibitor concentrations provided a K_i value of 0.080 μM.

To harmonize enzymatic data with insights deriving from the molecular modelling studies, the inhibitory activity of some enantiopure pyrrolidine derivatives under study was further evaluated towards human isoforms of AChE and BChE. Not any significant species-dependent difference was observed in the inhibition activity (see Table S1).

2.2.2. FAAH inhibition activity

Aiming to explore their potential as multitarget compounds, the whole series of pyrrolidine derivatives has also been tested for FAAH inhibition. FAAH is an important enzyme of the endocannabinoid system that degrades anandamide and oleamide, endogenous cannabinoid involved in reducing neuroinflammation and regulation of nervous activities such as memory and locomotion. Increased levels of brain FAAH expressions have been linked to increased AD-related symptoms,[19] making its inhibition an attractive strategy for the treatment of AD.

FAAH inhibition was measured via a fluorometric enzyme assay, including the well-known, potent FAAH inhibitor JZL195, as reference compound. The obtained data are reported in Table 1. All tested compounds were found to be active in the range 0.51–23.4 μM, thus performing as good FAAH inhibitors. Unlike what was found with cholinesterases, generally it was not possible to observe any stereoselective behavior of the pyrrolidine derivatives toward FAAH. An exception was represented by compound **9c**, bearing a 3,4-dimethoxy substituted phenyl ring as the aryloxy moiety and a naphthyl ring on the methylene spacer, being the *R*-isomer the eutomer, with an IC_{50} value of 1.8, which was 8-fold lower than that of its *S*-enantiomer. Even better activity was found in the *S*-isomer of compound **13f**, in which the aryloxy moiety is represented by a coumarin nucleus, that performed as the best FAAH inhibitor in the pyrrolidine series. Indeed, it showed an IC_{50} value of 0.51 μM, which was twice as active as its *R*-enantiomer. A noteworthy activity was also shown by the 4-phenyl substituted coumarin analogue, compound **14g**, which showed only a slight enantioselectivity in favor of the *S*-isomer with an IC_{50} value of 0.94, only two-fold lower than that of the *R*-isomer. While FAAH shows pronounced enantioselectivity towards inhibition by several chiral inhibitors,[20–22] the lack of a clearcut stereoselective behaviour among the pyrrolidine derivatives agrees with what was previously found in a series of aryloxy alkyl acids.[23]

2.2.3. Antioxidant activity

As extensively reported, AD is the outcome of a wide variety of highly interconnected factors. At the core of such a complex scenario, oxidative stress plays a key role in the progression of this disorder since it could trigger many pathological cascades. Thus, a multifunctional drug endowed with antioxidant capacity could more likely alter the course of the disease. In order to investigate the cytoprotective potential of all the compounds under study, the in vitro antioxidant activity was evaluated by means of the 2′,7′-dichlorodihydrofluorescein diacetate (DCFH-DA) cellular-based assay by measuring the reducing effect of the tested compounds against oxidation of 2′,7′-dichlorodihydrofluorescein (DCFH) induced by H_2O_2 to the fluorescent probe 2′,7′-dichlorofluorescein (DCF). Tests were performed on human hepatocellular liver carcinoma (HepG2) cells since they have an enhanced oxidative metabolism that causes cellular oxidative stress and/or generates reactive metabolites, making them well suited to study protection against oxidative and cytotoxic effects.[24] In addition, neuroblastoma SH-SY5Y cells have been used as a model for human neurons. Quercetin, a naturally occurring compound known to have strong antioxidant activity, has been used as reference molecule. The obtained results are summarized in Table 1. Almost all pyrrolidine derivatives significantly reduced H_2O_2-induced oxidation mainly on HepG2 cells. A clearcut stereoselective behaviour can be observed in almost all the active compounds, being, in most cases, the *R*-isomer the eutomer. Compounds bearing an electron rich aryl moiety (as the phenyl or the naphthyl ones) linked to the methylene spacer on the nitrogen atom generally showed eutomer IC_{50} values at least two-fold lower than those of the corresponding enantiomers. Conversely, the activity sharply decreased when the phenyl ring linked to the methylene spacer was substituted with electron-withdrawing groups as in compound **6a**. The *R*-isomer of compound **7a**, bearing a benzodioxole nucleus as the aryloxy moiety and a naphthyl ring on the methylene spacer, performed as the most active antioxidant compound in the pyrrolidine series on HepG2 cell lines, with IC_{50} value of 0.40, which was 160-fold lower than that of its *S*-enantiomer and significantly lower than that of the reference molecule quercetin (12.5 μM). The enantioselectivity was also evident for compound **11e**, bearing a *meta*-nitro substituted phenyl ring as the aryloxy moiety, with the *R*-isomer showing an IC_{50} value of 6.4, while the *S*-isomer was inactive. A slight enantioselectivity was found for the benzodioxole analogue of **7a**, compound **5a**, also in this case in favor of the *R*-isomer (IC_{50} = 19.7 μM) being the IC_{50} distomer/IC_{50} eutomer ratio of approximately 4. Concerning the SH-SY5Y cell, the pyrrolidine derivatives generally were less active toward this cell line with respect to the HepG2 cell line. Also in this case, compound **7a** performed as a potent antioxidant with an IC_{50} value of 8.4 μM for the *R*-isomer, showing the same stereoselectivity pattern even though with a lower index (the IC_{50} of the *S*-enantiomer is 31.2 μM). The most active compound toward this cell line was compound **6a** while it was less active

toward HepG2 cells. This benzodioxole analogue exhibited toward SH-SY5Y cells an IC_{50} value of 1.8 μM in favor of the *S*-enantiomer, performing noticeably more potent than the reference molecule. It is noteworthy for this compound a high stereoselectivity pattern with an index of 34, even though reversed with respect to what was generally observed, being in this case the *S*-isomer the eutomer. Once again, the size of the aryl ring seems related to the stereoselectivity pattern. As the oxidant activity of most of the tested compounds occurred in a stereoselective manner, with a significant difference between the enantiomers being observed in most cases, this result suggests that the antioxidant activity of the active compounds is structurally specific, it should stem from the interaction with at least one or more macromolecular target involved in the pharmacological outcome at the pharmacodynamic level. Although the exact molecular mechanism underlying this biological feature has not yet been unveiled, this data proved the role of pyrrolidine scaffold, particularly in conjunction with benzodioxole nucleus, in the inhibition of ROS mediated oxidative stress. Furthermore, to rule out the potential cytotoxicity of the tested compounds, a MTT assay was performed on both cell lines at different times (1 h and 24 h). When the cells were challenged with the tested compounds until the concentration of 100 μM, no cytotoxicity was observed at the times used for the assay towards both HepG2 and SH-SY5Y cells (data not shown). Since the cell viability was not affected, conceivably the pyrrolidine derivatives have a satisfactory safety profile.

2.3. Molecular modelling studies

2.3.1. Molecular dockings

The promising activities of compounds (*R*)-**7a**, (*S*)-**13f**, and (*S*)-**14g** prompted us to seek clues and directives for *in-silico* evaluation of the complementarity of the most active pyrrolidines against their respective targets. Hence, molecular docking to the catalytic site of the tested enzymes was performed, validating the resulting poses through a similarity study with known and potent esterase and amidase inhibitors whose bioactive conformations have already been assessed using X-ray crystallographic data.[25] We started from AChE that is well known with respect to its binding site location, extension and characterization, having on the molecular surface three hot spots, named respectively catalytic triad (CT Ser203, Glu334, His447), catalytic anionic site (CAS Trp86 and Phe338) and the peripheral anion site (PAS Tyr72, Tyr124 and Trp286), where ligands are anchored and produce favourable interactions with the enzyme, as indeed observed in the X-ray complex of donepezil with hAChE. Considering the best derivative (*R*)-**7a**, a binding mode consistent to the donepezil one was achieved. As depicted in Fig. 4, the protonated nitrogen nucleus is sited close to the CT and orients the large aromatic pendant just below Trp86 stabilizing the links to the target surface with a strong and extended *face-to-face* π-π stacking. At the other end of the molecular scaffold the chiral carbon helps the polar moiety of the ligand to be directed at the opening of the less hindered AChE active center gorge, recruiting two hydrogen bonds with Tyr124 sidechain and Phe295 backbone. Notable, the benzodioxole nucleus cope the binding throughout additional π-π stackings with the aromatic residues Trp286, Phe297 and Tyr341.

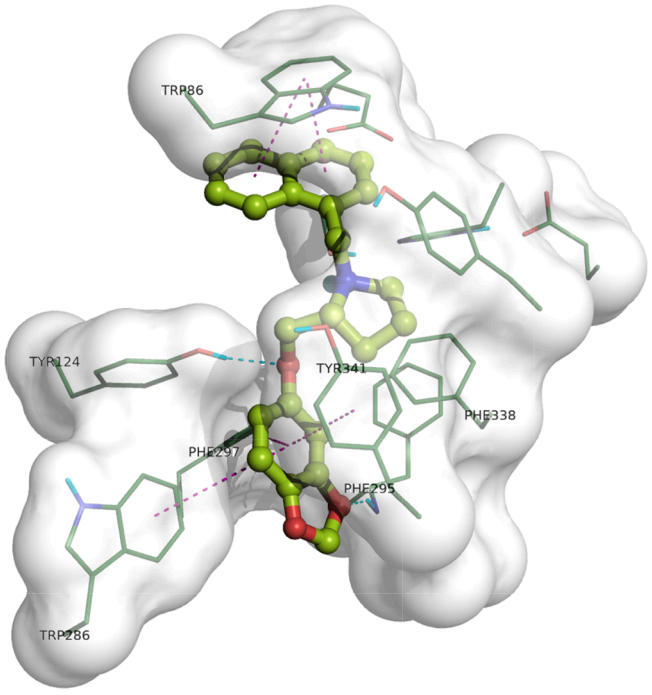

Fig. 4. Binding mode for (*R*)-**7a** to the AChE active site. In the interaction pattern scheme, hydrogen bonds and π-π stackings are depicted in cyan and magenta respectively. (For interpretation of the references to colour in this figure legend, the reader is referred to the web version of this article.)

Contrarily to this strongly inhibiting pyrrolidine, the same highly directional and properly oriented contacts cannot be produced by the enantiomer (*S*)-**7a**, that indeed is poorly (~30 % of the eutomer potency) able to lower the enzyme activity. Docking scores reported in Table 2 corroborated these results since the ESP rule figures (see methods) of (*R*)-**7a** are very close in terms of binding energy, ligand efficacy and molecular similarity to donepezil, and they are able then to explain the ability of (*R*)-**7a** to efficiently inhibit AChE. Afterwards, we challenged the BChE by the most potent compound (*S*)-**14g** and, in this instance, a tight replication of the previously discussed binding poses was hampered by some differences in CT, CAS, and PAS aminoacidic composition and accessible surface of the active sites, as well as by the opposite chiral configuration, and the larger hindrance and flexibility of the coumarine analog eutomer. In fact, a more bended conformation, largely replicating the crystallographic structure of this enzyme bound to a potent tacrine-methylanacardate hybrid inhibitor (**TKN**), was obtained.[26] Notable is the role of the coumarin ring since this system is able to recruit one hydrogen bond with the indole of Trp430 by mean of the carbonyl fragment and, at the same time, the phenyl substituent in the position 4 of the same ring produces stackings with Trp82 part of the CAS anchoring point for butyrylcholinesterase,in addition to, a nonconventional '*OH···π*' interaction is gained from the same 4-phenyl and the hydroxyl of Ser198.[27] A proper hydrogen bond is otherwise generated between the charged nitrogen and the Pro285 backbone, while the naphthalene ring makes *edge-to-face* π-π contacts withTrp231, Phe329 and Phe398 (see Fig. 5).

The same indications, gained from the previously reported docking scores, are indeed observed for BChE (see Table 2).

The last docking concerned (*S*)-**13f**, namely the unsubstituted congener of the aforementioned derivative (*S*)-**14g**, that is the most active FAAH inhibitor. With respect to this latest enzyme, it must be

Table 2
AChE, BChE and FAAH ligands docking scores.

Target		FEB[a]	ΔE[b]	EFF[c]	TAN[d]	POP[e]
AChE[d]	(*R*)-**7a**	–10.23	0.51	–0.379	0.681	73/1000
	donepezil	–10.83	0.05	–0.387	1.279	470/100
BChE[e]	(*S*)-**14g**	–11.70	0.00	–0.334	0.505	11/1000
	TKN	–8.65	0.25	–0.247	1.174	21/100
FAAH[f]	(*S*)-**13f**	–9.17	0.95	–0.316	0.574	42/1000
	JZL195	–10.22	1.02	–0.319	nd	20/100

[a]**FEB** Free Energy of Binding; [b]**ΔE** Energy difference between the selected pose and the relative global minimum; [c]**EFF** Ligand efficacy; [d]**TAN** Tanimoto Combo similarity coefficient of with X-ray poses; [e]**POP** Cluster members population; [d]pdb entry 6O4W,[24] [e] pdb entry 7BGC,[25] [f]pdb entry 4DO3.[28]

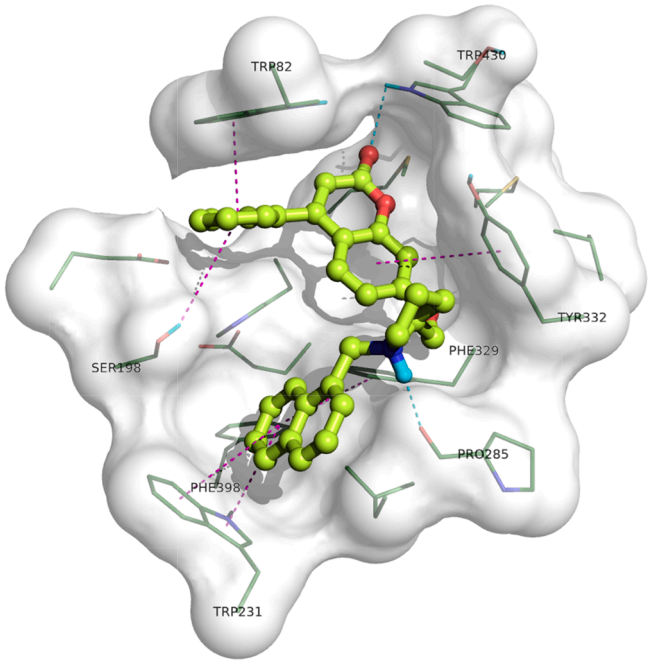

Fig. 5. Binding mode for (*S*)-**14g** to the BChE active site. In the interaction pattern scheme, hydrogen bonds and π-π stackings are depicted in cyan and magenta, respectively. (For interpretation of the references to colour in this figure legend, the reader is referred to the web version of this article.)

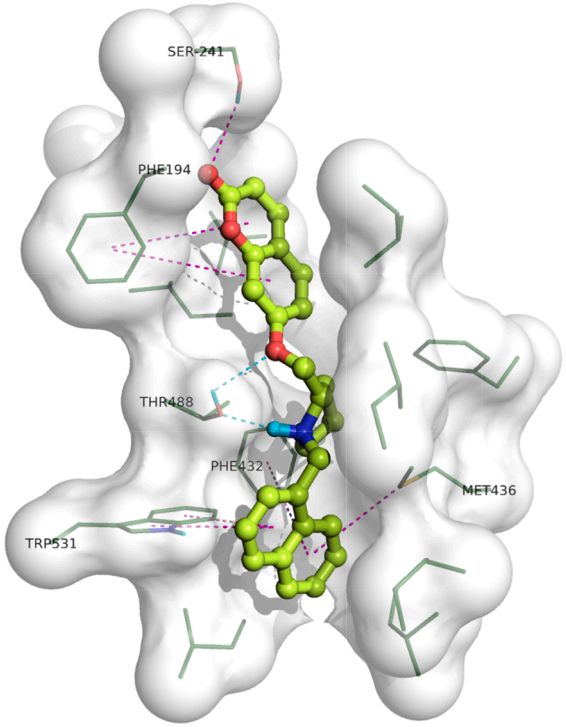

Fig. 6. Binding mode for (*S*)-**13f** to the FAAH active site. In the interaction pattern scheme, hydrogen bonds and π-π stackings are depicted in cyan and magenta respectively. (For interpretation of the references to colour in this figure legend, the reader is referred to the web version of this article.)

pointed out a membrane-accessing tunnel, comprising in a phenylalanine and a tryptophan residue, followed by an elongated cavity that gives access to an unusual catalytic triad performing the hydrolysis of substrates, made up by two serines and one lysine, as perceived from crystallographic data. As long as this is observed, (*S*)-**14g** then is fully extended along the active site channel, and because of this, more than one hydrogen bond are produced: a first one involves the coumarinic carbonyl, in cooperation with Phe194, and the catalytic Ser241, a second bond enrols Thr488 side chain and the oxygen linking atom, while a third, charged reinforced, recruits in this instance the same threonine bonding to pyrrolidine ring. The terminal aromatic end of our inhibitor locks the entry channel of the amidase making additional hydrophobic and aromatic contacts with Phe432, Met436 and Trp531 as shown in Fig. 6.

Overall, in all the three previously presented instances, a good match between molecular dockings and X-ray determined binding poses was achieved, as it might be perceived from the overlay with donepezil, TKN and JZL195. This result allows us to identify for our most promising pyrrolidines the main determinants needed to acquire an efficient profile as AChE/BChE and FAAH inhibitors, as proved by robust figures given by the *in-silico* binding mode simulations as well as by molecular comparison with known inhibitors selected and reference compounds (see Fig. S1).

2.3.2. Molecular dynamics

As an ex-post analysis, we also decided to run molecular dynamics (MD) simulations on (*R*)-**7a** and (*S*)-**14g** with AChE and BChE active sites, respectively, trying to assess the persistence and stability of the ligand-enzyme complexes and to depict at the same time the proper structural features that better modulate targets inhibition. To achieve these tasks, visuals like MD trajectory flow, as well as plots and diagrams endowing insights on molecular complexes fluctuations and/or stabilization (i.e. RMSD, Radius of Gyration), largely helps the examination of discovered binding modes, dynamic ligand-interaction patterns, and contacts tenacity to the studied binding site, assessing then the anchoring or steering a binder with respect to the target molecule and/or catalytic site. Using as inputs the docking poses relative to each pyrrolidine derivative, the dynamic trajectories for AChE/(*R*)-**7a** and BChE/(*S*)-**14g** complexes were therefore produced, while FAAH/(*S*)-**13f** was not examined due to the detrimental 1–31 N-terminal residues truncation, a critical moiety relative to the single-pass membrane of the protein. From the reported plots it might be perceived that after almost a third (>600 ns) of the MD run both complexes reached a significantly stable molecular assembly as emerged form a lower RMSD fluctuation (see Fig. 7) and by a standard deviation from the mean values for protein and ligand equal to ±0.35 and ±0.46, and ±0.52 and ±1.05 Ang respectively for AChE/(*R*)-**7a** and BChE/(*S*)-**14g** complexes.

The lone difference in the two plots refers to a different, and lower, RMSD measured in the last 500 ns of the (*S*)-**14g** run**,** probably due to an alternative binding mode explored in the sampling of the ligand and enzyme conformational space, and the same information is also confirmed in Fig. 8 where the bar plots show the distribution of the Radius of Gyration values, endowing the distance of the whole molecular complexes from its barycenter indicating then the protein structure compactness and its folding persistence. Indeed, only the (*S*)-**14g** MR run shows a skewed frequency, with a first peak at 4.6 and a second shifted to 5.20 value of gyration.

This evidence might be most likely ascribed to the extent in the accessible surface of this latter enzyme that is larger sized comparing to AChE gorge whose cavity is about 200 $Å^3$ smaller than the BChE.[29] Furthermore, the analysis of interaction diagrams (Fig. 9) suggests some interesting topics: in AChE/(*R*)-**7a** complex it is intriguing the role of a water molecule able to bridge the charged nitrogen of pyrrolidine with His447, one of the essential residue of CT, as well as the involvement of Tyr337 making persistent aromatic interactions with the aromatic ring of the inhibitor, and on the other hand, in BChE complex it noteworthy the evidence of multiple contacts gained by Trp82 and the coumarinic moiety of (*S*)-**14g**, as well as the intervention of two different water molecules helping the ligand binding.

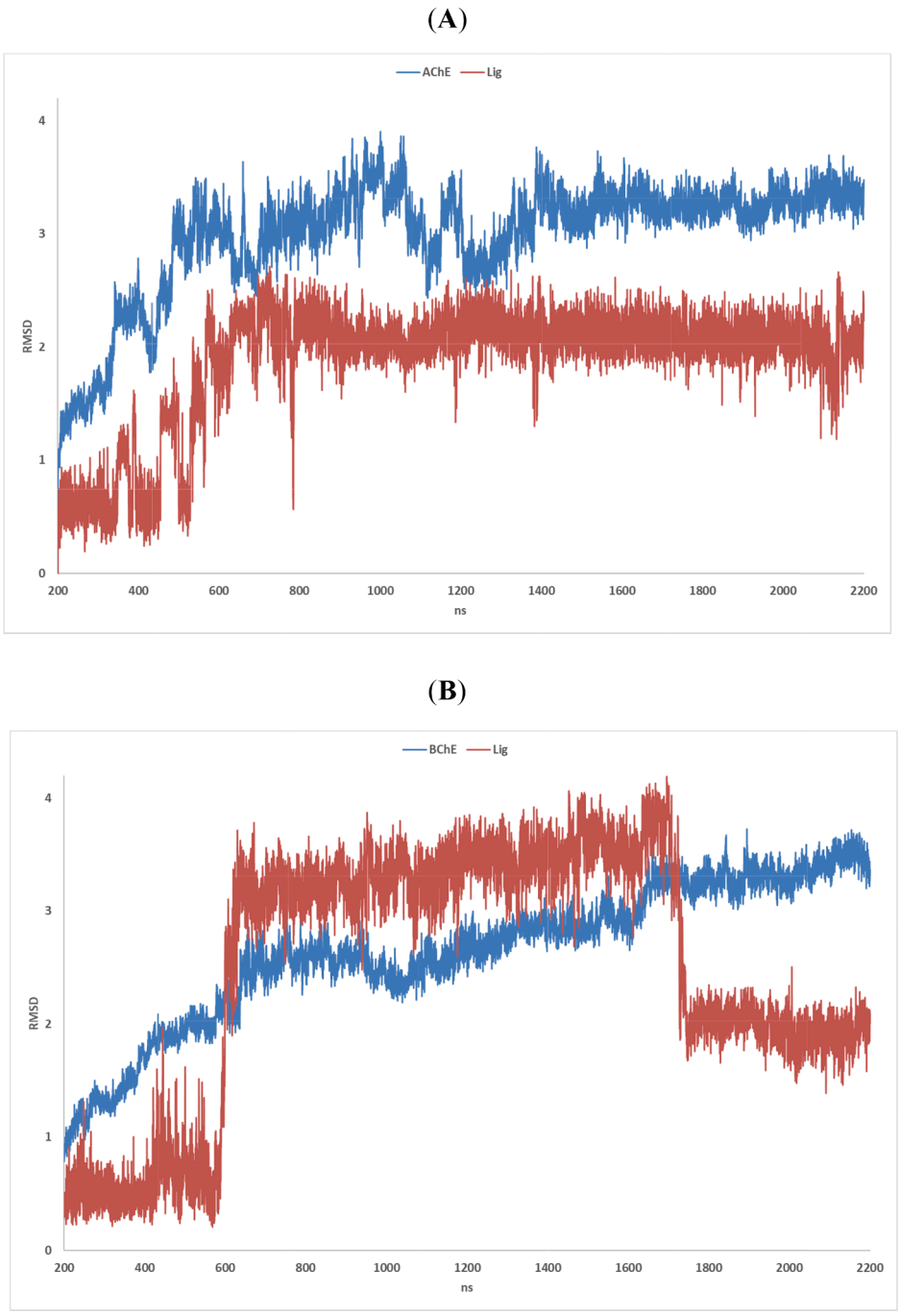

Fig. 7. Timeline plots of the Cα-trace RMSD calculated from the AChE/(*R*)-**7a** (**A**) and BChE/(*S*)-**14g** (**B**) complexes MD trajectories. Protein and ligand values are drawn in blue and red respectively. (For interpretation of the references to colour in this figure legend, the reader is referred to the web version of this article.)

2.4. ADME properties

The Brain or Intestinal Estimate permeation method was used for drug-likeness predictions.[30] As shown in Fig. 10, all compounds in the series might be well absorbed in the gastrointestinal tract (white region of the plot), so they spot in the white ellipse of the BOILED-Egg plot. Moreover, all the studied compounds, with the exception of the **14g** enantiomers, could potentially permeate the blood brain barrier (yellow region).

Next, the interaction and affinity with human serum albumin (has, K_D values) for the most active compounds (*R*)-**7a** and (*S*)-**14g** were determined by surface plasmon resonance (SPR) using the well-known HSA strong binder warfarin as standard reference (K_D = 5.50 ± 0.33 μM).[31] HSA represents the most abundant protein in plasma and plays a relevant role in affecting the ADME profiles of xenobiotics. The binding curves showed that the response at equilibrium was quite rapidly reached for each of the tested compounds. Compounds (*R*)-**7a** (K_D = 3.60 ± 0.20 μM) and (*S*)-**14g** (K_D = 5.75 ± 0.15 μM) appeared as strong HSA binders, thus showing (*R*)-**7a** affinity to HSA higher than warfarin. By considering the physiological HSA concentration in plasma (680 μM), at 10 μM concentration all compounds were predicted to be highly bound to albumin.[31]

Finally, the active compounds with respect to the protein targets, i.e. (*R*)-**7a**, (*S*)-**14g** (esterases), and (*S*)-**13f** (FAAH), were estimated experimentally on their membrane permeability using Parallel Artificial Membrane Permeability Assay (PAMPA). The results were compared to

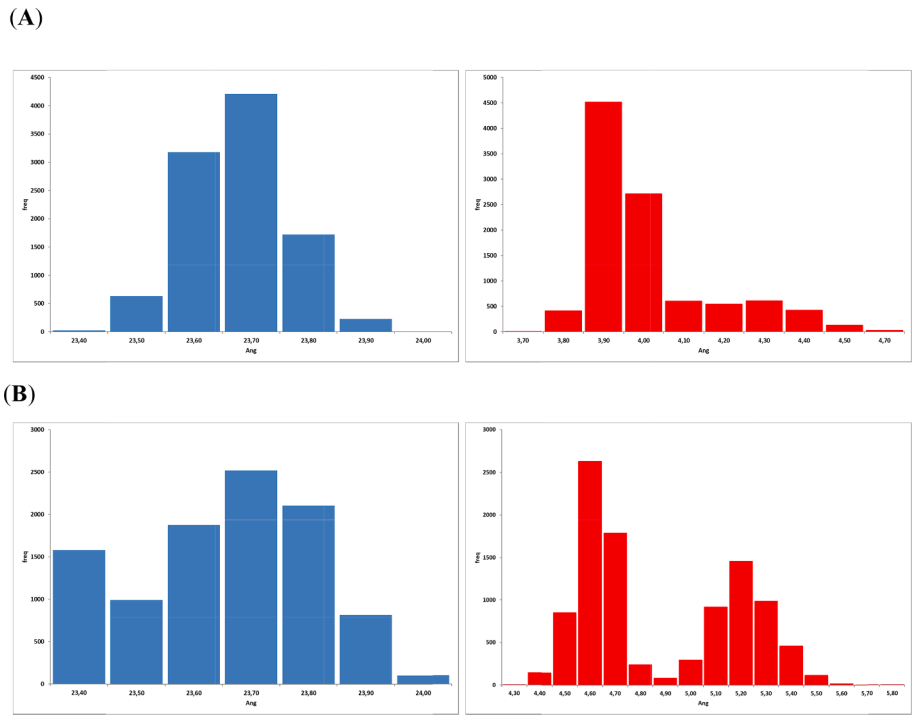

Fig. 8. Bar plots of the Radius of Gyration distribution values in the AChE/(*R*)-**7a** (**A**) and BChE/(*S*)-**14g** (**B**) complexes MD trajectories. Protein and ligand data are drawn in blue and red respectively. (For interpretation of the references to colour in this figure legend, the reader is referred to the web version of this article.)

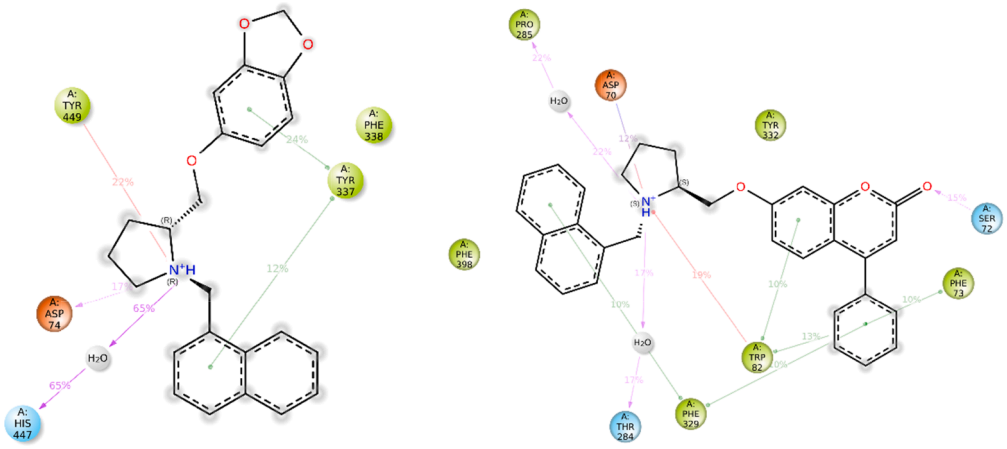

Fig. 9. Simulation interactions diagrams for (*R*)-**7a** (left) and (*S*)-**14g** (right) with AChE and BChE binding sites, respectively. The minimum contact strengths shown are at least 10 % of trajectories length from 200 to 2200 ns.

the well-permeable caffeine and expressed as a permeability coefficient (*Pe*) calculated according to formulas provided by PAMPA plate manufacturer (Table 3). Among the tested compounds, (*S*)-**14g** was able to cross properly artificial barrier as its $Pe = 2.01 \times 10^{-6}$ cm/s was above the recommended by the PAMPA manufacturer threshold for the permeable compounds ($Pe = 1.5 \times 10^{-6}$ cm/s).[32] On the other hand, compound (*R*)-**7a** was not found in acceptor wells and *Pe* for (*S*)-**13f** was lower than the manufacturer's recommended value for permeable compounds (Table 3).

3. Conclusion

Twenty novel pyrrolidine containing derivatives were obtained and tested in more than one enzymatic assay resulting as innovative molecular entities with a promising framework for targeting and inhibiting cholinesterases, in conjunction with other critical molecular targets implicated in neurodegenerative diseases. In particular, the coumarin but more originally the sesamol scaffolds, proved to be endowed with promising chemical solutions as proved by valuable inhibition profiles of (*R*)-**7a**, and (*S*)-**14g** on esterases, and (*S*)-**13f** on FAAH. Moreover, 10 enantiomer pairs were also acquired, revealing in some instances chirality influences on the efficacy of enzyme inhibition. As additional neuroprotective ability, (*R*)-**7a** also performed out as excellent antioxidant, even more potent than quercetin. Molecular modelling studies, performed with both dockings and dynamics, marked the main molecular determinants giving mandatory effects for stable and effective interaction with the tested molecular targets, in particular AChE and BChE. The results of PAMPA showed that the dual BChE/FAAH inhibitor, compound (*S*)-**14g**, having a relatively highest chance of penetrating the brain, performed, among the three most interesting analogues, as the best CNS drug-likeness compound to further investigate for the potential therapy of neurodegenerative diseases.

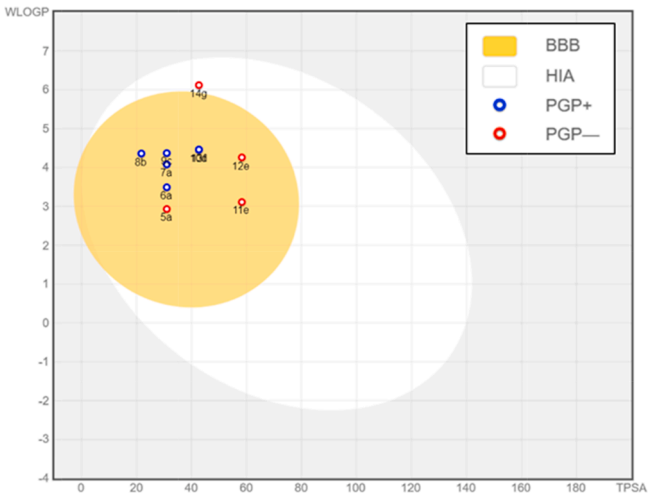

Fig. 10. Prediction of pharmacokinetic properties of compounds under study according to BoiledEgg. **BBB** = blood–brain barrier permeation; **HIA** = human intestinal absorption; **PGP+** = not P-gp substrate; **PGP–** = P-gp substrate.

Table 3
Permeability of (*R*)-**7a**, (*S*)-**13f** and (*S*)-**14g** determined in PAMPA.

Cmpd.	***Pe**** (10^{-6} cm/s) ± SD
Caffeine	6.33 ± 1.15
(*R*)-**7a**	not permeable*
(*S*)-**13f**	0.26 ± 0.09
(*S*)-**14g**	2.01 ± 0.82

* Compound was not observed in the acceptor wells of PAMPA plate.

4. Experimental protocols

4.1. Chemistry

Chemicals were purchased from Sigma-Aldrich or Alpha-Aesar at the highest quality commercially available. Compounds (*R*)- and (*S*)-**2** were prepared as previously reported.[17] Compounds (*R*)- and (*S*)-**3b**,**3d**,**4b**,**4d**,**8b**,**10d** were previously described.[11] Yields refer to purified products and were not optimized. The structures of the compounds were confirmed by routine spectrometric and spectroscopic analyses. Only spectra for compounds not previously described are given. Melting points were determined on a Gallenkamp apparatus in open glass capillary tubes and are uncorrected. ^{1}H NMR and ^{13}C NMR spectra were recorded on either a Varian VX Mercury spectrometer operating at 300 and 75 MHz for ^{1}H and ^{13}C, respectively, or an AGILENT 500 MHz operating at 500 and 126 MHz for ^{1}H and ^{13}C, respectively, using $CDCl_3$ or CD_3OD as solvent. Chemical shifts (δ) are reported in ppm relative to the residual non-deuterated solvent resonance: $CDCl_3$, $\delta = 7.26$ (^{1}H NMR) and $\delta = 77.3$ (^{13}C NMR),CD_3OD, $\delta = 3.30$ (^{1}H NMR) and $\delta = 47.8$ (^{13}C NMR) as internal references. Coupling constants (*J*) are given in Hz. Gas chromatography (GC)/mass spectroscopy (MS) was performed on an AGILENT 6890N–5973N MSD spectrometer. HRMS analyses were performed using an AGILENT 6530 accurate mass Q-TOF spectrometer. Elemental analyses were performed on a Eurovector Euro EA 3000 analyzer and the data for C, H, N were within ±0.4 of theoretical values. Optical rotations were measured on a PerkinElmer Mod 341 spectropolarimeter,concentrations are expressed in g 100 mL¢1, and the cell length was 1 dm; thus, $[\alpha]_D^{20}$ values are given in units of 10^{-1} degcm^{2}g^{-1}. Chromatographic separations were performed on silica gel columns by column chromatography on silica gel (Kieselgel 60, 0.040–0.063 mm, Merck, Darmstadt, Germany). TLC analyses were performed on precoated silica gel on aluminum sheets (Kieselgel 60 F254, Merck).

*4.1.1. General procedure for the preparation of 2-aryloxymethyl substituted pyrrolidine-1-carboxylate (**3a–g**)*

A solution of diisopropyl azodicarboxylate (DIAD, 10.0 mmol, 1.5 eq) in dry THF (35 mL) was added dropwise to a solution of (*R*)-**2** (1.3 g, 6.7 mmol, 1 eq), proper aryl alcohol (10.0 mmol, 1.5 eq) and triphenylphosphine (2.6 g, 10.0 mmol, 1.5 eq) in dry THF (50 mL) under N_2 atmosphere at room temperature. The reaction mixture was stirred overnight and then was concentrated in vacuo. Et_2O was added to the residue and the solid filtered off. The filtrate was evaporated, and the residue was purified by silica gel column chromatography (eluent AcOEt/hexane 2:8).

*4.1.1.1. (R)-tert-Butyl 2-{[(2H-1,3-benzodioxol-5-yl)oxy]methyl}pyrrolidine-1-carboxylate **[(R)-3a]**.* Yield: 25 %; slight yellow oil; $[\alpha]_D^{20} = +55$ (*c* 2, $CHCl_3$); GC–MS: (70 eV) *m/z* (%) 321 (M^+, 2), 70 (100); ^{1}H NMR (500 MHz, $CDCl_3$): δ 1.46 (s, 9H, CH_3), 1.75–2.05 (m, 4H), 3.25–3.45 (m, 2H), 3.65–3.88 (m, 1H), 3.94–4.17 (m, 2H), 5.89 (s, 2H), 6.34 (s, 1H), 6.50 (s, 1H), 6.65 – 6.70 (m, 1H); ^{13}C NMR (126 MHz, $CDCl_3$): δ 23.8 (1C), 28.5 (3C), 46.8 (1C), 55.9 (1C), 68.9 (1C), 69.3 (1C), 79.8 (1C), 98.1 (1C), 101.08 (1C), 105.7 (1C), 107.9 (1C), 145.3 (1C), 148.1 (1C), 152.2 (1C), 151.5 (1C).

*4.1.1.2. (S)-tert-Butyl 2-{[(2H-1,3-benzodioxol-5-yl)oxy]methyl}pyrrolidine-1-carboxylate **[(S)-3a]**.* Yield: 28 %; slight yellow oil; $[\alpha]_D^{20} = -50$ (*c* 2, $CHCl_3$); spectrometric and spectroscopic data agreed with those reported for the *R* enantiomer.

*4.1.1.3. (R)-tert-Butyl 2-[(3,4-dimethoxyphenoxy)methyl]pyrrolidine-1-carboxylate **[(R)-3c]**.* Yield: 63 %; transparent oil; $[\alpha]_D^{20} = +53.5$ (*c* 2, $CHCl_3$); GC–MS: (70 eV) *m/z* (%) 337 (M^+, 5.5), 154 (100); ^{1}H NMR (300 MHz, CDCl3): δ 1.46 (s, 9H), 1.80–2.07 (m, 4H), 3.30–3.50 (m, 2H), 3.65–3.80 (m,1H), 3.82 (s, 3H), 3.85 (s, 3H), 3.96–4.20 (m, 2H), 6.37–6.60 (m, 2H), 6.75 (d, $J = 8.7$ Hz, 1H); ^{13}C NMR (126 MHz, CDCl3): δ 22.9 (1C), 23.8 (1C), 28.5 (3C), 46.7 (1C), 55.8 (1C), 56.0 (1C), 56.5 (1C), 68.7 (1C), 79.6 (1C), 100.7 (1C), 103.9 (1C), 112.0 (1C), 143.4 (1C), 149.8 (1C), 153.4 (1C), 154.6 (1C).

*4.1.1.4. (S)-tert-Butyl 2-[(3,4-dimethoxyphenoxy)methyl]pyrrolidine-1-carboxylate **[(S)-3c]**.* Yield 53 %; transparent oil; $[\alpha]_D^{20} = -56$ (*c* 2, $CHCl_3$); spectrometric and spectroscopic data agreed with those reported for the *R* enantiomer.

*4.1.1.5. (R)-tert-Butyl 2-[(3-nitrophenoxy)methyl]pyrrolidine-1-carboxylate **[(R)-3e]**.* Yield 72 %; pale yellow oil; $[\alpha]_D^{20} = +48$ (c 1.8, $CHCl_3$); GC–MS: (70 eV) *m/z* (%) 322 (M^+ <1), 70 (100); ^{1}H NMR (500 MHz, CD_3OD): δ 1.54 (s, 9H), 1.80–2.18 (m, 4H), 3.27–3.67 (m, 2H), 3.67–4.10 (m, 1H), 4.1–4.45 (m, 2H), 6.92–7.51 (m, 1H), 7.51–7.95 (m, 3H); ^{13}C NMR (126 MHz, $CDCl_3$) δ 18.2 (1C), 19.1 (1C), 23.4 (1C), 23.7 (1C), 23.8 (1C), 41.93 (1C), 51.1 (1C), 64.0 (1C), 75.3 (1C), 104.8 (1C), 110.9 (1C), 116.4 (1C), 125.2 (1C), 144.5 (1C). 152.7 (1C). 154.6 (1C).

*4.1.1.6. (S)-tert-Butyl 2-[(3-nitrophenoxy)methyl]pyrrolidine-1-carboxylate **[(S)-3e]**.* Yield: 56 %; pale yellow oil; $[\alpha]_D^{20} = -62$ (*c* 2, $CHCl_3$); spectrometric and spectroscopic data agreed with those reported for the *R* enantiomer.

*4.1.1.7. (R)-tert-Butyl 2-{[(2-oxo-2H-1-benzopyran-7-yl)oxy]methyl}pyrrolidine-1-carboxylate **[(R)-3f]**.* Yield: 59 %; dark-yellow oil; $[\alpha]_D^{20} = +24.9$ (*c* 2, $CHCl_3$); GC–MS: (70 eV) *m/z* (%) 245 ($M^+ - 100 < 1$), 70 (100); ^{1}H NMR (300 MHz, $CDCl_3$): δ 1.46 (s, 9H), 1.83–2.08 (m, 4H), 3.27–3.48 (m, 2H), 3.80–4.0 (m, 1H), 4.02–4.27 (m, 2H), 6.23 (d, $J = 9.5$ Hz, 1H), 6.73–6.96 (m, 2H), 7.35 (d, $J = 8.4$, 1H), 7.62 (d, $J = 9.5$ Hz, 1H); ^{13}C NMR (126 MHz, $CDCl_3$): δ 22.9 (1C), 23.8 (1C), 28.5 (3C),

47.0 (1C), 68.5 (1C), 69.0 (1C), 70.0 (1C), 102.0 (1C), 112.6 (1C), 112.8 (1C), 113.1 (1C), 128.7 (1C), 143.3 (1C), 155.8 (1C), 156.3 (1C), 161.2 (1C), 162.0 (1C).

4.1.1.8. (S)-tert-Butyl 2-{[(2-oxo-2H-1-benzopyran-7-yl)oxy]methyl}pyrrolidine-1-carboxylate ***[(S)-3f]***. Yield 57 %; dark-yellow oil; $[\alpha]_D^{20}$ = –25.1 (*c* 2, $CHCl_3$); spectrometric and spectroscopic data agreed with those reported for the *R* enantiomer.

4.1.1.9. (R)-tert-Butyl 2-{[(2-oxo-4-phenyl-2H-1-benzopyran-7-yl)oxy]methyl}pyrrolidine-1-carboxylate ***[(R)-3g]***. Yield: 61 %; brown oil; $[\alpha]_D^{20}$ = +35 (*c* 2, $CHCl_3$); GC–MS: (70 eV) *m/z* (%) 321 (M^+ –100, <1), 70 (100); ^{1}H NMR (300 MHz, $CDCl_3$): δ 1.47 (s, 9H), 1.81–2.02 (m, 4H), 3.25–3.50 (m, 2H), 3.76–4.36 (m, 3H), 6.21 (s, 1H), 6.75–6.85 (m, 1H), 6.87–6.95 (m, 1H), 7.37 (d, *J* = 8.9 Hz, 1H), 7.40–7.46 (m, 2H), 7.47–7.56 (m, 3H); ^{13}C NMR (126 MHz, $CDCl_3$): δ 14.2 (1C), 21.7 (1C), 23.2 (3C), 28.5 (1C), 32.6 (1C), 60.4 (1C), 68.5 (1C), 102.4 (1C), 104.3 (1C), 112.1 (1C), 113.5 (1C), 127.9 (1C), 128.4 (2C), 128.8 (2C), 129.5 (1C), 135.7 (1C), 135.6 (1C), 155.6 (1C), 155.7 (1C), 160.3 (1C), 161.3 (1C).

4.1.1.10. (S)-tert-Butyl 2-{[(2-oxo-4-phenyl-2H-1-benzopyran-7-yl)oxy]methyl}pyrrolidine-1-carboxylate ***[(S)-3g]***. Yield 26 %; brown oil; $[\alpha]_D^{20}$ = –27 (*c* 2, $CHCl_3$); spectrometric and spectroscopic data agreed with those reported for the *R* enantiomer.

*4.1.2. General procedure for the preparation of 2-aryloxymethyl substituted pyrrolidines (****4a–g****)*

To solution of proper 2-aryloxymethyl substituted pyrrolidine-1-carboxylate (4 mmol) in CH_2Cl_2 (10 mL), CF_3COOH (10 mL) was added, and the mixture was stirred at room temperature for 24 h. The solvent was evaporated in vacuo, and the residue was taken up with H_2O and EtOAc and extracted three times with 2 N HCl. The aqueous phases were collected, made alkaline and then extracted three times with EtOAc. The combined extracts were dried (anhyd Na_2SO_4) and evaporated in vacuo.

4.1.2.1. (R)-2-{[(2H-1,3-Benzodioxol-5-yl)oxy]methyl}pyrrolidine ***[(R)-4a]***. Yield: 51 %; slight yellow oil; $[\alpha]_D^{20}$ = +1 (*c* 2, $CHCl_3$); GC–MS: (70 eV) *m/z* (%) 221 (M^+, 3), 70 (100); ^{1}H NMR (500 MHz, $CDCl_3$): δ 1.45–1.58 (m, 1H), 1.70–1.85 (m, 2H), 1.86–1.96 (m, 1H), 2.68 (brs, 1H), 2.87–2.95 (m, 1H), 2.95–3.04 (m, 1H), 3.39–3.49 (m, 1H), 3.77 (dd, *J* = 9.1, 6.9 Hz, 1H), 3.83 (dd, *J* = 9.1, 4.8 Hz, 1H), 5.88 (s, 2H), 6.30 (dd, *J* = 8.5, 2.5 Hz 1H), 6.48 (d, *J* = 2.5 Hz, 1H), 6.67 (d, *J* = 8.5 Hz, 1H); ^{13}C NMR (126 MHz, $CDCl_3$): δ 25.1 (1C), 27.9 (1C), 46.5 (1C), 57.4 (1C), 72.0 (1C), 98.1 (1C), 100.1 (1C), 105.7 (1C), 107.9 (1C), 141.6 (1C), 148.2 (1C), 154.4 (1C).

4.1.2.2. (S)-2-{[(2H-1,3-Benzodioxol-5-yl)oxy]methyl}pyrrolidine ***[(S)-4a]***. Yield: 44 %; slight yellow oil; $[\alpha]_D^{20}$ = –1 (*c* 2, $CHCl_3$); spectrometric and spectroscopic data agreed with those reported for the *R* enantiomer.

4.1.2.3. (R)-2-[(3,4-Dimethoxyphenoxy)methyl]pyrrolidine ***[(R)-4c]***. Yield: 79 %; brown oil; $[\alpha]_D^{20}$ = –1.4 (*c* 2, $CHCl_3$); GC–MS: (70 eV) *m/z* (%) 237 (M^+, 4.0), 70 (100); ^{1}H NMR (500 MHz, $CDCl_3$): δ 1.81–1.88 (m, 1H), 1.90–1.98 (m, 1H), 1.99–2.14 (m, 2H), 3.11–3.23 (m, 2H), 3.75–3.83 (m overlapping s at 3.81 and s at 3.82, 1H), 3.81 (s, 3H), 3.82 (s, 3H), 4.00–4.08 (m, 2H), 6.35 (dd, *J* = 8.7, 2.8 Hz, 1H), 6.48 (br s, 1H), 6.55 (d, *J* = 2.7 Hz, 1H), 6.72 (d, *J* = 8.8 Hz, 1H). ^{13}C NMR (126 MHz, $CDCl_3$): δ 24.0 (1C), 27.0 (1C), 45.4 (1C), 55.8 (1C), 56.4 (1C), 58.3 (1C), 68.0 (1C), 101.3 (1C), 103.9 (1C), 111.7 (1C), 144.1 (1C), 149.8 (1C), 152.6 (1C).

4.1.2.4. (S)-2-[(3,4-Dimethoxyphenoxy)methyl]pyrrolidine ***[(S)-4c]***. Yield 84 %; brown oil; $[\alpha]_D^{20}$ = +1.3 (*c* 2, $CHCl_3$); spectrometric and spectroscopic data agreed with those reported for the *R* enantiomer.

4.1.2.5. (R)-2-[(3-Nitrophenoxy)methyl]pyrrolidine ***[(R)-4e]***. Yield 83 %; orange oil; $[\alpha]_D^{20}$ = – 7.5 (c 2, $CHCl_3$); GC–MS: (70 eV) *m/z* (%) 222 (M^+ <1), 70 (100); ^{1}H NMR (500 MHz, CD_3OD): δ 1.52–164 (m, 1H), 1.74–1.93 (m, 2H), 1.95–2.02 (m, 1H), 2.52 (br s, 1H exch D_2O), 2.94–3.09 (m, 2H), 3.51–3.62 (m, 1H),), 3.93 (dd, *J* = 9.0, 7.0 Hz, 1H), 4.01 (dd, *J* = 9.0, 4.7 Hz, 1H), 7.23 (ddd, *J* = 8.3, 2.5, 0.9 Hz, 1H), 7.41 (t, *J* = 8.2 Hz, 1H), 7.73 (t, *J* = 2.3 Hz, 1H), 7.81 (ddd, *J* = 8.1, 2.1, 0.9 Hz, 1H); ^{13}C NMR (126 MHz, $CDCl_3$) δ 25.3 (1C), 28.0 (1C), 46.6 (1C), 57.0 (1C), 72.0 (1C), 108.9 (1C), 115.8 (1C), 121.6 (1C), 129.9 (1C), 149.2 (1C), 159.5 (1C).

4.1.2.6. (S)-2-[(3-Nitrophenoxy)methyl]pyrrolidine ***[(S)-4e]***. Yield 71 %; orange oil; $[\alpha]_D^{20}$ = +11 (*c* 2, $CHCl_3$); spectrometric and spectroscopic data agreed with those reported for the *R* enantiomer.

4.1.2.7. (R)-7-[(Pyrrolidin-2-yl)methoxy]-2H-1-benzopyran-2-one ***[(R)-4f]***. Yield: 36 %; brown oil; $[\alpha]_D^{20}$ = +42.2 (*c* 2, $CHCl_3$); GC–MS: (70 eV) *m/z* (%) 245 (M^+, 1), 70 (100); ^{1}H NMR (500 MHz, $CDCl_3$): δ 1.51–2.19 (m, 4H), 2.82–3.82 (m, 2H), 3.34–3.76 (m, 1H), 3.34–3.76 (m, 1H), 3.85–4.08 (m, 1H), 4.94 (dd, *J* = 12.1, 6.0 Hz, 1H), 6.22 (d, *J* = 9.4 Hz, 1H), 6.79 (s, 1H), 6.84 (d, *J* = 8.2 Hz, 1H), 7.34 (d, *J* = 8.5 Hz, 1H), 7.61 (d, *J* = 9.4 Hz, 1H); ^{13}C NMR (126 MHz, $CDCl_3$): δ 21.9 (1C), 46.4 (1C), 57.0 (1C), 70.0 (1C), 71.4 (1C), 101.6 (1C), 112.6 (1C), 112.8 (1C), 113.1 (1C), 128.7 (1C), 143.4 (1C), 155.8 (1C), 161.2 (1C), 162.0 (1C).

4.1.2.8. (S)-7-[(Pyrrolidin-2-yl)methoxy]-2H-1-benzopyran-2-one ***[(S)-4f]***. Yield 38 %; brown oil; $[\alpha]_D^{20}$ = –41.2 (*c* 2, $CHCl_3$); spectrometric and spectroscopic data agreed with those reported for the *R* enantiomer.

4.1.2.9. (R)-4-Phenyl-7-[(pyrrolidin-2-yl)methoxy]-2H-1-benzopyran-2-one ***[(R)-4g]***. Yield: 26 %; brown oil; $[\alpha]_D^{20}$ = +4.2 (*c* 2, $CHCl_3$); GC–MS: (70 eV) *m/z* (%) 321 (M^+, <1), 70 (100); ^{1}H NMR (500 MHz, $CDCl_3$): δ 1.69–2.10 (m, 4H), 2.92–3.12 (m, 3H), 3.58 (d, *J* = 5.5 Hz, 1H), 3.87–4.04 (m, 2H), 6.20 (s, 1H), 6.79 (dd, *J* = 8.9, 2.4 Hz, 1H), 6.88 (d, *J* = 2.3 Hz, 1H), 7.35 (d, *J* = 8.9 Hz, 1H), 7.42 (dt, *J* = 6.0, 3.1 Hz, 2H), 7.48–7.51 (m, 3H); ^{13}C NMR (126 MHz, $CDCl_3$): δ 22.0 (1C), 27.9 (1C), 46.5 (1C), 57.0 (1C), 101.8 (1C), 111.9 (1C), 112.6 (2C), 127.9 (1C), 128.4 (2C), 128.8 (2C), 129.6 (1C), 135.5 (2C), 155.8 (1C), 155.9 (1C), 161.2 (1C), 162.1 (1C).

4.1.2.10. (S)-4-Phenyl-7-[(pyrrolidin-2-yl)methoxy]-2H-1-benzopyran-2-one ***[(S)-4g]***. Yield 41 %; brown oil; $[\alpha]_D^{20}$ = –4.6 (*c* 2, $CHCl_3$); spectrometric and spectroscopic data agreed with those reported for the *R* enantiomer.

*4.1.3. General procedure for the preparation of the final compounds (****5a–7a, 8b, 9c, 10d, 11e, 12e, 13f, 14g****)*

A solution of the proper arylmethyl bromide (2.4 mmol, 1.2 eq) in 7 mL of abs EtOH was added dropwise to a magnetically stirred solution of the proper 2-aryloxymethyl substituted pyrrolidine (2 mmol, 1 eq) and Et_3N (4 mmol, 2 eq) in absolute EtOH (20 mL). The solution was stirred at room temperature. After 24 h, the excess EtOH was evaporated under reduced pressure, and the residue was dissolved in EtOAc and washed with water and brine. The organic layer was dried (anhyd Na_2SO_4) and evaporated *under vacuum*. The residue was purified by column chromatography using silica gel (eluent: EtOAc/hexane 1:9).

4.1.3.1. (R)-2-[(1,3-Benzodioxol-5-yloxy)methyl]-1-benzylpyrrolidine ***[(R)-5a]***. Yield 66 %; slight yellow oil; $[\alpha]_D^{20}$ = +56 (*c* 2, $CHCl_3$); GC–MS: (70 eV) *m/z* (%) 311 (M^+ <1), 160 (100); ^{1}H NMR (300 MHz, $CDCl_3$): δ 1.65–1.81 (m, 3H), 1.88–2.13 (m, 1H), 2.20–2.40 (m, 1H), 2.90–3.07 (m, 2H), 3.51 (d, *J* = 13.0 Hz, 1H), 3.83 (ddd, *J* = 15.7, 9.2,

5.9 Hz, 2H), 4.12 (d, $J = 13.0$ Hz, 1H), 5.90 (s, 2H), 6.29 (dd, $J = 8.4$, 2.4 Hz, 1H), 6.48 (d, $J = 2.4$ Hz, 1H), 6.69 (d, $J = 8.4$ Hz, 1H), 7.15–7.44 (m, 5H); ^{13}C NMR (75 MHz, $CDCl_3$): δ 23.0 (1C), 28.7 (1C), 54.7 (1C), 59.8 (1C), 62.4 (1C), 72.6 (1C), 98.1 (1C), 101.0 (1C), 105.7 (1C), 107.9 (1C), 126.9 (1C), 128.2 (2C), 128.9 (2C), 139.6 (1C), 141.5 (1C), 148.2 (1C), 154.6 (1C). ESI-HRMS *m/z* $[C_{13}H_{21}NO_3 + H]^+$ calcd 312.1594, found 312.1600.

4.1.3.2. (S)-2-[(1,3-Benzodioxol-5-yloxy)methyl]-1-benzylpyrrolidine ***[(S)-5a]***. Yield 45 %; slight yellow oil; $[\alpha]_D^{20} = -60$ (*c* 2, $CHCl_3$); spectrometric and spectroscopic data were in agreement with those reported for the *R* enantiomer.

4.1.3.3. (R)-2-[(1,3-Benzodioxol-5-yloxy)methyl]-1-(2-fluorobenzyl)pyrrolidine ***[(R)-6a]***. Yield 37 %; brown oil; $[\alpha]_D^{20} = -7.5$ (*c* 2, $CHCl_3$); GC–MS: (70 eV) *m/z* (%) 329 (M^+ <1), 109 (100); ^{1}H NMR (500 MHz, $CDCl_3$) δ 1.34–1.45 (m, 1H), 1.52–1.65 (m, 1H), 1.67–1.83 (m, 2H), 1.96–2.06 (m, 1H), 2.11–2.27 (m, 1H), 2.68–2.76 (m, 1H), 2.94–3.10 (m, 2H), 3.66 (s, 1H), 3.77–3.98 (m, 1H), 4.16–4.25 (m, 1H), 5.90 (t, $J =$ 3.5 Hz, 2H), 6.29–6.41 (m, 1H), 6.49 (d, $J = 2.3$ Hz, 1H), 7.03 (t, $J = 9.1$ Hz, 1H), 7.06–7.12 (m, 1H), 7.19–7.27 (m, 1H), 7.35 (t, $J = 7.5$, Hz, 1H); ^{13}C NMR (126 MHz, $CDCl_3$) δ 23.1 (1C), 29.9 (1C), 52.8 (1C), 55.1 (1C), 57.5 (1C), 74.4 (1C), 99.8 (1C), 101.1 (1C), 107.9 (1C), 108.2 (1C), 115.1 (1C), 123.8 (1C), 128.9 (1C), 131.5 (1C), 141.8 (1C), 148.2 (1C), 152.7 (1C). 160.4 (1C), 162.4 (1C); ESI-HRMS *m/z* $[C_{19}H_{20}FNO_3 + H]^+$ calcd 330.1500, found 330.1505.

4.1.3.4. (S)-2-[(1,3-Benzodioxol-5-yloxy)methyl]-1-(2-fluorobenzyl)pyrrolidine ***[(S)-6a]***. Yield 68 %; yellow oil; $[\alpha]_D^{20} = +4.2$ (*c* 2.5, $CHCl_3$); spectrometric and spectroscopic data agreed with those reported for the *R* enantiomer.

4.1.3.5. (R)-2-[(1,3-Benzodioxol-5-yloxy)methyl]-1-(naphthalen-1-ylmethyl)pyrrolidine ***[(R)-7a]***. Yield 83 %; transparent oil; $[\alpha]_D^{20} = +15$ (*c* 2, $CHCl_3$); GC–MS: (70 eV) *m/z* (%) 361 (M^+ <1), 141 (100); ^{1}H NMR (500 MHz, $CDCl_3$) δ 1.65–1.77 (m, 4H), 2.00–2.08 (m, 1H), 2.32–2.40 (m, 1H), 2.85–2.92 (m, 1H), 3.04–3.09 (m, 1H), 3.79–3.94 (m, 2H), 4.65 (d, $J = 12.9$ Hz, 1H), 5.90 (s, 2H), 6.29 (dd, $J = 8.5$, 2.5 Hz, 1H), 6.47 (d, $J = 2.5$ Hz, 1H), 6.68 (d, $J = 8.5$ Hz, 1H), 7.36–7.49 (m, 4H), 7.73–7.85 (m, 2H), 8.34 (dd, $J = 9.1$, 7.5 Hz, 1H); ^{13}C NMR (126 MHz, $CDCl_3$) δ 23.1 (1C), 28.6 (1C), 55.1 (1C), 58.4 (1C), 63.1 (1C), 72.6 (1C), 98.1 (1C), 101.1 (1C), 105.8 (1C), 107.9 (1C), 124.7 (1C), 125.1 (1C), 125.2 (1C), 125.8 (1C), 126.9 (1C), 127.8 (1C), 128.3 (1C), 132.3 (1C), 133.8 (1C), 135.7 (1C), 141.5 (1C), 148.2 (1C), 154.5 (1C); ESI-HRMS *m/z* $[C_{23}H_{23}NO_3 + H]^+$ calcd 362.1751, found 362.1759.

4.1.3.6. (S)-2-[(1,3-Benzodioxol-5-yloxy)methyl]-1-(naphthalen-1-ylmethyl)pyrrolidine ***[(S)-7a]***. Yield 75 %; transparent oil; $[\alpha]_D^{20} = -14.8$ (*c* 2, $CHCl_3$); spectrometric and spectroscopic data were in agreement with those reported for the *R* enantiomer.

4.1.3.7. (R)-2-[(3,4-Dimethoxyphenoxy)methyl]-1-(naphthalen-1-ylmethyl)pyrrolidine ***[(R)-9c]***. Yield 58 %; light yellow oil; $[\alpha]_D^{20} = +7.1$ (*c* 2, $CHCl_3$); GC–MS: (70 eV) *m/z* (%) 377 (M^+ <1), 141 (100); ^{1}H NMR (500 MHz, $CDCl_3$) δ 1.65–1.81 (m, 4H), 2.02–2.07 (m, 1H), 2.33–2.43 (m, 1H), 2.87–2.96 (m, 1H), 3.07–3.12 (m, 1H), 3.82 (s, 3H), 3.84 (s, 3H), 3.85–3.91 (m, 1H), 3.95 (dd, $J = 9.1$, 5.7 Hz, 1H), 4.70 (d, $J = 12.9$ Hz, 1H), 6.37 (dd, $J = 8.7$, 2.8 Hz, 1H), 6.51 (d, $J = 2.8$ Hz, 1H), 6.77 (d, $J = 8.7$ Hz, 1H), 7.35–7.51 (m, 4H), 7.76 (d, $J = 8.2$ Hz, 1H), 7.83 (d, $J =$ 8.7 Hz, 1H), 8.37 (d, $J = 8.3$ Hz, 1H); ^{13}C NMR (126 MHz, $CDCl_3$) δ 23.1 (1C), 28.7 (1C), 55.1 (1C), 55.8 (1C), 56.5 (1C), 58.4 (1C), 63.1 (1C), 72.2 (1C), 100.9 (1C), 103.7 (1C), 111.8 (1C), 124.7 (1C), 125.2 (1C), 125.5 (1C), 125.8 (1C), 126.9 (1C), 127.8 (1C), 128.3 (1C), 132.3 (1C), 133.8 (1C), 135.8 (1C), 143.4 (1C), 149.8 (1C), 153.6 (1C); ESI-HRMS *m/z* $[C_{24}H_{27}NO_3 + H]^+$ calcd 378.2064, found 378.2079.

4.1.3.8. (S)-2-[(3,4-Dimethoxyphenoxy)methyl]-1-(naphthalen-1-ylmethyl)pyrrolidine ***[(S)-9c]***. Yield 26 %; light yellow oil; $[\alpha]_D^{20} = -6.7$ (*c* 1.2, $CHCl_3$); spectrometric and spectroscopic data were in agreement with those reported for the *R* enantiomer.

4.1.3.9. (R)-1-Benzyl-2-[(3-nitrophenoxy)methyl]pyrrolidine ***[(R)-11e]***. Yield 76 %; slight yellow oil; $[\alpha]_D^{20} = +40$ (*c* 2, $CHCl_3$); GC–MS: (70 eV) *m/z* (%) 312 (M^+ <1), 160 (100); ^{1}H NMR (500 MHz, $CDCl_3$): δ 1.70–1.92 (m, 4H), 1.97–2.11 (m, 1H), 2.26–2.44 (m, 1H), 2.91–3.18 (m, 1H), 3.59 (t, $J = 12.8$ Hz, 1H), 3.84–3.93 (m, 1H), 3.94–4.03 (m, 1H), 4.06–4.14 (m, 1H), 7.16–7.20 (m, 1H), 7.23– 7.28 (m, 1H), 7.32 (t, $J = 7.5$ Hz, 2H), 7.36 (d, $J = 7.3$ Hz, 2H), 7.38–7.43 (m, 1H), 7.71 (t, $J =$ 2.1 Hz, 1H), 7.77–7.84 (m, 1H); ^{13}C NMR (126 MHz, CD_3OD) δ 23.2 (1C). 28.7 (1C), 54.8 (1C), 59.9 (1C), 62.1 (1C), 72.1 (1C), 109.0, (1C), 115.6 (1C), 121.5 (1C), 127.0 (1C), 128.5 (2C), 128.9 (2C), 129.8 (1C), 139.5 (1C), 149.2 (1C), 159.6 (1C); ESI-HRMS *m/z* $[C_{18}H_{20}N_2O_3 + H]^+$ calcd 313.1547, found 313.1552.

4.1.3.10. (S)-1-Benzyl-2-[(3-nitrophenoxy)methyl]pyrrolidine ***[(S)-11e]***. Yield 74 %; slight yellow oil; $[\alpha]_D^{20} = -51$ (*c* 2, $CHCl_3$); spectrometric and spectroscopic data were in agreement with those reported for the *R* enantiomer.

4.1.3.11. (R)-1-(Naphthalen-1-ylmethyl)-2-[(3-nitrophenoxy)methyl]pyrrolidine ***[(R)-12e]***. Yield 69 %; slight yellow oil; $[\alpha]_D^{20} = +7$ (*c* 2, $CHCl_3$); GC–MS: (70 eV) *m/z* (%) 362 (M^+ <1), 141 (100); ^{1}H NMR (500 MHz, CD_3OD): δ 2.05–2.15 (m, 2H), 2.25–2.36 (m, 1H), 2.47–2.60 (m, 1H), 3.32 (dt, $J = 3.3$, 1.6 Hz, 1H), 3.45–3.69 (m, 2H), 4.31–4.7 (m, 3H), 4.91 (d, $J = 13.6$ Hz, 1H), 5.31 (d, $J = 13.5$ Hz, 1H), 7.34 (dd, $J = 8.3$, 2.5 Hz, 1H), 7.50–7.62 (m, 3H), 7.71 (t, $J = 2.3$ Hz, 1H), 7.83 (dd, $J =$ 7.1, 1.1 Hz, 1H), 7.88–7.93 (m, 1H), 7.95 – 7.99 (m, 1H, Ar), 8.02 (d, J = 8.3 Hz, 1H), 8.20–8.27 (m, 1H, Ar); ^{13}C NMR (126 MHz, CD_3OD) δ 26.0 (1C), 30.2 (1C), 59.6 (1C), 60.0 (1C), 70.2 (1C), 70.8 (1C), 113.2 (2C), 120.3 (1C), 124.7 (1C), 126.5 (1C), 129.1 (1C), 130.3 (1C), 131.2 (1C), 132.8 (1C), 134.3 (1C), 134.7 (1C), 134.8 (1C), 135.5 (1C), 138.0 (1C), 153.1 (1C), 161.9 (1C); ESI-HRMS *m/z* $[C_{22}H_{22}N_2O_3 + H]^+$ calcd 363.1709, found 363.1701.

4.1.3.12. (S)-1-(Naphthalen-1-ylmethyl)-2-[(3-nitrophenoxy)methyl]pyrrolidine ***[(S)-12e]***. Yield 80 %; slight yellow oil; $[\alpha]_D^{20} = -4$ (*c* 2, $CHCl_3$); spectrometric and spectroscopic data agreed with those reported for the *R* enantiomer.

4.1.3.13. (R)-7-{[1-(Naphthalen-1-ylmethyl)pyrrolidin-2-yl]methoxy}-2H-chromen-2-one ***[(R)-13f]***. Yield 81 %; light yellow oil; $[\alpha]_D^{20} = +65$ (*c* 0.8, $CHCl_3$); GC–MS: (70 eV) *m/z* (%) 385 (M^+ 2), 141 (100); ^{1}H NMR (300 MHz, $CDCl_3$) δ 1.66–1.87 (m, 4H), 1.96–2.16 (m, 1H), 2.34–2.50 (m, 1H), 2.86–3.0 (m, 1H), 3.14 (td, $J = 10.7$, 5.5 Hz, 1H), 3.82–4.01 (m, 2H), 4.58 (d, $J = 12.8$ Hz, 1H), 6.24 (d, $J = 9.5$ Hz, 1H), 6.75 (dt, $J = 5.9$, 2.4 Hz, 2H), 7.32 (d, $J = 8.5$ Hz, 1H), 7.36–7.49 (m, 4H), 7.61 (d, $J = 9.5$ Hz, 1H), 7.73–7.86 (m, 2H), 8.31 (dd, $J = 8.2$, 6.6 Hz, 1H); ^{13}C NMR (126 MHz, $CDCl_3$): δ 21.9 (1C), 27.2 (1C), 30.9 (1C), 53.8 (1C), 64.8 (1C), 70.1 (1C), 102.6 (1C), 112.2 (1C), 113.6 (1C), 113.9 (1C), 122.7 (1C), 125.5 (2C), 126.5 (1C), 127.6 (1C), 129.2 (2C), 129.4 (1C), 132.3 (1C), 133.9 (2C), 143.2 (2C), 155.6 (1C), 160.8 (1C). ESI-HRMS *m/z* $[C_{25}H_{23}NO_3 + H]^+$ calcd 386.1751 found 386.1762.

4.1.3.14. (S)-7-{[1-(Naphthalen-1-ylmethyl)pyrrolidin-2-yl]methoxy}-2H-chromen-2-one ***[(S)-13f]***. Yield 86 %; light-yellow oil; $[\alpha]_D^{20} = -45$ (*c* 2, $CHCl_3$); spectrometric and spectroscopic data were in agreement with those reported for the *R* enantiomer.

4.1.3.15. (R)-7-{[1-(Naphthalen-1-ylmethyl)pyrrolidin-2-yl]methoxy}-4-phenyl-2H-chromen-2-one ***[(R)-14g]***. Yield 88 %; light yellow oil; $[\alpha]_D^{20}$ = –4.5 (*c* 1, $CHCl_3$); GC–MS: (70 eV) *m/z* (%) 461 (M^+ <1), 141 (100);

^{1}H NMR (500 MHz, $CDCl_3$) δ 1.62–1.84 (m, 3H), 2.05–2.15 (m, 1H), 2.39–2.47 (m, 1H), 2.86–3.01 (m, 1H), 3.14 (td, J = 10.6, 5.5 Hz, 1H), 3.85–4.00 (m, 3H), 4.58 (d, J = 12.9 Hz, 2H), 6.22 (s, 1H), 6.72 (dd, J = 8.9, 2.5 Hz, 1H), 6.81 (d, J = 2.5 Hz, 1H), 7.34 (d, J = 8.9 Hz, 1H), 7.36–7.49 (m, 5H), 7.50–7.52 (m, 3H), 7.67–7.87 (m, 2H), 8.24–8.37 (m, 1H); ^{13}C NMR (126 MHz, $CDCl_3$) δ 23.2 (1C), 28.7 (1C), 55.2 (1C), 58.5 (1C), 62.6 (1C), 72.0 (1C), 101.7 (1C), 111.8 (1C), 112.5 (1C), 112.7 (1C), 124.5 (1C), 125.2 (1C), 125.6 (1C), 125.8 (1C), 126.9 (1C), 127.9 (2C), 128.4 (3C), 128.8 (2C), 129.5 (1C), 132.3 (1C), 133.8 (1C), 135.5 (1C), 135.6 (1C), 155.8 (1C), 160.0 (1C), 161.3 (1C), 162.2 (1C). ESI-HRMS m/z $[C_{13}H_{27}NO_3 + H]^+$ calcd 462.2064 found 462.2060.

4.1.3.16. (S)-7-{[1-(Naphthalen-1-ylmethyl)pyrrolidin-2-yl]methoxy}-4-phenyl-2H-chromen-2-one ***[(S)-14g]***. Yield 60 %, light-yellow oil; $[\alpha]_D^{20}$ = +2.8 (*c* 3, $CHCl_3$); spectrometric and spectroscopic data were in agreement with those reported for the *R* enantiomer.

*4.1.4. General procedure for the preparation of the hydrohalide salts of the final compounds (**6a, 7a, 9c, 11e, 12e**)*

A small amount of the proper hydrohalide (2 M HCl or 2 M HBr) was added to the free base and H_2O was removed azeotropically. The crude solid was recrystallized from EtOH/Et_2O.

4.1.4.1. (R)-2-[(1,3-Benzodioxol-5-yloxy)methyl]-1-(2-fluorobenzyl)pyrrolidine hydrochloride ***[(R)-6a·HCl]***. Yield 30 %; slight yellow crystals: mp 172–173 °C (abs EtOH/Et_2O); $[\alpha]_D^{20}$ = –37 (*c* 2.2, MeOH); Anal. ($C_{19}H_{21}ClFNO_3 \cdot 0.5H_2O$) C, H, N.

4.1.4.2. (S)-2-[(1,3-Benzodioxol-5-yloxy)methyl]-1-(2-fluorobenzyl)pyrrolidine hydrochloride ***[(S)-6a·HCl]***. Yield 51 %; slight yellow crystals: mp 175–177 °C (abs EtOH /Et_2O); $[\alpha]_D^{20}$ = +36 (*c* 2, MeOH); Anal. ($C_{19}H_{21}ClFNO_3 \cdot 0.33H_2O$) C, H, N.

4.1.4.3. (R)-2-[(1,3-Benzodioxol-5-yloxy)methyl]-1-(naphthalen-1-ylmethyl)pyrrolidine hydrochloride ***[(R)-7a·HCl]***. Yield 35 %; slight yellow crystals: mp 198–200 °C (abs EtOH/Et_2O); $[\alpha]_D^{20}$ = –53 (*c* 1, MeOH); Anal. ($C_{23}H_{24}ClNO_3 \cdot 0.33H_2O$) C, H, N.

4.1.4.4. (S)-2-[(1,3-Benzodioxol-5-yloxy)methyl]-1-(naphthalen-1-ylmethyl)pyrrolidine hydrochloride ***[(S)-7a·HCl]***. Yield 41 %; slight yellow crystals: mp 200–202 °C (abs EtOH/Et_2O); $[\alpha]_D^{20}$ = +50 (*c* 1, MeOH); Anal. ($C_{23}H_{24}ClNO_3 \cdot 0.75H_2O$) C, H, N.

4.1.4.5. (R)-2-[(3,4-dimethoxyphenoxy)methyl]-1-(naphthalen-1-ylmethyl)pyrrolidine hydrochloride ***[(R)-9c·HCl]***. Yield 62 %, off-white crystals: mp: 169–171 °C (abs. EtOH/Et_2O); $[\alpha]_D^{20}$ = –56 (*c* 1, MeOH); Anal. ($C_{24}H_{27}NO_3 0.8HCl$) C, H, N.

4.1.4.6. (S)-2-[(3,4-Dimethoxyphenoxy)methyl]-1-(naphthalen-1-ylmethyl)pyrrolidine hydrochloride ***[(S)-9c·HCl]***. Yield 54 %, off-white crystals: mp: 168–170 °C (abs. EtOH/Et_2O); $[\alpha]_D^{20}$ = +61 (*c* 1, MeOH); Anal. ($C_{24}H_{28}ClNO_3$) C, H, N.

4.1.4.7. (R)-1-Benzyl-2-[(3-Nitrophenoxy)methyl]pyrrolidine hydrobromide ***[(R)-11e·HBr]***. Yield 51 %; yellow crystals: mp 80–81 °C (abs EtOH/Et_2O); $[\alpha]_D^{20}$ = –20 (*c* 2.1, MeOH); Anal. ($C_{18}H_{21}BrN_2O_3 \cdot 0.5H_2O$) C, H, N.

4.1.4.8. (S)-1-benzyl-2-[(3-Nitrophenoxy)methyl]pyrrolidine hydrobromide ***[(S)-11e·HBr]***. Yield 43 %; yellow crystals: mp 81–83 °C (abs EtOH/Et_2O); $[\alpha]_D^{20}$ = +14 (*c* 2, MeOH); Anal. ($C_{18}H_{21}BrN_2O_3$) C, H, N.

4.1.4.9. (R)-1-(Naphthalen-1-ylmethyl)-2-[(3-nitrophenoxy)methyl]pyrrolidine hydrobromide ***[(R)-12e·HBr]***. Yield 60 %; white crystals: mp 169–170 °C (abs EtOH/Et_2O); $[\alpha]_D^{20}$ = +87 (*c* 2.1, MeOH); Anal. ($C_{22}H_{23}BrN_2O_3 \cdot 0.7\ H_2O$) C, H, N.

4.1.4.10. (S)-1-(Naphthalen-1-ylmethyl)-2-[(3-nitrophenoxy)methyl]pyrrolidine hydrobromide ***[(S)-12e·HBr]***. Yield 56 %; white crystals: mp 169–170 °C (abs EtOH/Et_2O); $[\alpha]_D^{20}$ = –86 (*c* 2, MeOH); Anal. ($C_{22}H_{23}BrN_2O_3$) C, H, N.

4.1.5. Preparation of 1-(bromomethyl)naphthalene ***(16)***

PBr_3 (1.89 g, 7.0 mmol) was added dropwise to commercial naphthalen-1-ylmethanol (**15**) (1 g, 6.3 mmol) cooled in an ice bath. The mixture was stirred for 2 h at 0 °C and then at room temperature for 24 h. At the end, the mixture was poured into ice and extracted three times with EtOAc. The organic layer was dried (anhyd Na_2SO_4) and evaporated under vacuum. The desired product was obtained as a yellow oil (1.075 g). Yield: 77 %; GC–MS: (70 eV) m/z (%) 220 (M^+, 7), 141 (100). Spectroscopic data were in agreement with those reported in the literature.[33]

4.2. Biology

4.2.1. Cholinesterases inhibition assay

The inhibiton activites of the studied compounds toward electric eel AChE and horse BChE (Sigma-Aldrich), were assessed by following the Ellman's method, with slight modifications, on a 96-wells plate system.[34–36] The BChE activity was determined in a reaction mixture containing 20 μL of a AChE solution (2 U/mL in 0.1 M pH 8.0 phosphate buffer, PB), 20 μL of 5,5-dithio-bis-(2-nitrobenzoic) acid (DTNB 3.3 mM in 0.1 M pH 7.0 PB, containing 0.1 mM $NaHCO_3$), 20 μL of a solution of the test compound (ranging from 1×10^{-4} to 1×10^{-9} M in 0.1 M pH 8.0 PB), and 120 μL of pH 8.0 PB. After 20 min incubation at 25 °C, the substrate acetylthiocholine iodide (20 μL, 0.05 mM solution in PB) was added, and its hydrolysis rate was monitored for 10 min at 412 nm. The concentration of compound which produced 50 % inhibition of the AChE activity (IC_{50}) was calculated by nonlinear regression of the response/concentration (log) curve, by using Prisma GraphPad software (ver. 5.01), thus plotting the initial rate values. The BChE inhibitory activity was similarly determined, by instead using a solution of BChE (3 U/mL in 0.1 M pH 8.0 PB), and butyrylthiocholine iodide (0.05 mM) as enzyme and substrate, respectively. The inhibition data are reported as means of IC_{50} values determined at least in three independent measurements.

4.2.2. FAAH inhibition activity

Inhibition of FAAH was measured in 96-well black flat-bottom microtiter NBS plates (COSTAR flat black), using a final volume of 200 μL in each well. Pre-incubation of solutions at decreasing concentrations of every compound with the enzyme (FAAH Human recombinant, Cayman Chemical, Ann Arbor, MI, USA) occurred in a bespoke buffer (tris-HCl 125 mM, $Na_2EDTA \cdot 2H_2O$ 1 mM, pH = 9.0) for ten minutes at room temperature, under orbital shaking. Afterwards 50 μL of a substrate (7-amino-4-methyl2H-1-benzopyran-2-one-5Z,8Z,11Z,14Z-eicosatetraenamide, at a final concentration of 5 μM) were added. The final concentration of DMSO in the assay mix was 5 %. Plate reader Tecan Infinite M1000 Pro (Tecan, Cernusco S.N., Italy), was used to incubate each plate at 37 °C, while fluorescence values from each well were acquired every 30 s (λex = 340 nm, λem = 450 nm). Enzyme- or self-mediated substrate hydrolysis resulted in fluorescence emission, measured as relative fluorescence units (RFU). The results were normalized using control wells lacking any inhibitor and blank wells lacking both inhibitor and enzyme to calculate percent inhibition values for each well. IC_{50} values are expressed as mean ± SEM of at least two independent measurements performed in triplicate.[37]

4.2.3. Details for antioxidant activity studies

4.2.3.1. Culture cells. Human hepatocellular liver carcinoma (HepG2) cell line and human neuroblastoma cell line, SH-SY5Y, were purchased from the American Type Culture Collection (ATCC, Manassas, VA, USA), maintained at 37 °C in a humidified atmosphere with 95 % air and 5 % CO_2, and periodically screened for contamination. HepG2 cells were cultured in Eagle's Minimum Essential Medium (MEM), supplemented with 10 % Fetal Bovine Serum (FBS), 1 % L-glutamine, 100 U/mL penicillin/streptomycin, 1 % Non-Essential Amino Acids (NEAA). SH-SY5Y cells were grown in a 1:1 mixture of Dulbecco's modified Eagle's medium (DMEM)—high glucose and Ham's F12 Medium supplemented with 10 % FBS, 1 % L-glutamine and 100 U/mL penicillin/streptomycin. For cell assays, cells were trypsinized using Trypsin-EDTA 1X in PBS. Culture medium and reagents were purchased from Euroclone S.p.A., Pero, MI, Italy.

4.2.3.2. Dichlorofluorescein assay. Generation of ROS was monitored using an oxidation-sensitive fluorescent probe, 2′,7′-dichlorodihydrofluorescein diacetate (DCFH-DA, D6665; Sigma-Aldrich, St. Louis, MO) by slightly modifying the procedure reported by Wang et al.[38] Briefly, viable cells were seeded in a black 96-well cell culture plate (Costar, Sigma-Aldrich, St. Louis, MO, USA) and after 24 h were incubated with different concentrations (0.1–100 μM) of the tested compounds for 1 h at 37 °C in 5 % CO_2. DCFH-DA (25 μM final concentration) in medium without serum was added directly to each well, and the plate was incubated at 37 °C for 30 min at 37 °C in 5 % CO_2. After washing using PBS, 100 μM H_2O_2 in medium without serum was added to each well and the cells were incubated for an additional 30 min. The formation of fluorescent dichlorofluorescein (DCF) due to oxidation of DCFH in the presence of ROS, was read at 530 nm using a microplate reader TECAN M1000 PRO (Thermo Fisher Scientific, Waltham, MA, USA) and DMSO medium was used for control cells. At least three independent experiments with three replicates were carried out. Data were analyzed using Graphpad Prism 8.

4.2.3.3. Cell viability assay. HepG2 and SH-SY5Y cell viability was assessed by using a conventional 3-(4,5-dimethylthiazol-2-yl)-2,5-diphenyltetrazolium bromide (MTT) assay as previously reported.[39] Briefly, viable cells were seeded and grown for 24 h in a complete medium into a sterile 96-well cell culture cluster (Corning, Sigma-Aldrich, St. Louis, MO, USA) and maintained at 37 °C in a humidified atmosphere with 5 % CO_2. Subsequently, the cells were exposed to different concentrations of the compounds under investigation for a period of 1 h or 24 h. At the end, the culture medium was replaced by a solution of 0.5 mg/mL MTT (Sigma-Aldrich, St. Louis, MO, USA) in PBS. After 2 h of incubation at 37 °C in 5 % CO_2, the supernatant was carefully removed from each well, and the formazan crystals were dissolved in DMSO (Sigma-Aldrich, St. Louis, MO, USA). The absorbance values were measured at 570 nm using a TECAN M1000 pro using DMSO medium as blank solution. The cell viability was calculated according to the following formula: % cell viability = [optical density (OD) of tested compound/medium OD of control cells] × 100. Data were analysed using Graphpad Prism 8.

4.3. Molecular modelling studies

Ligands and enzymes structures were prepared and selected similarly to what reported in our previously published paper focused on the same targets, and the same also applies to the chosen docking protocol.[40] Targets selected for dockings were the enzyme-inhibitor complexes of AChE (chain A,pdb code 6O4W), BChE (pdb code 7BGC), and FAAH (pdb code 4DO3). Binding poses were ranked by **ESP**, a simple energy-, similarity- and population-based rule where **E** accounts for the free energy of binding, the energy difference between the selected pose and the relative global minimum and the ligand efficacy, **S** the similarity as scored by the Tanimoto_Combo coefficient according to the shape matching algorithm ROCS [OpenEye Scientific Software, ROCS, 3.4.0.4, OpenEye Scientific Software, Santa Fe, NM, https://www.eyesopen.com], **P** is the cluster member population, considering valid the rule once at least four out of five parameters are below a certain figure. In this instance, dockings were filtered applying the ESP rule with thresholds values equal to **FEB** < –9.00, **ΔE** < 2.00, **EFF** < –0.300, **SIM** > 0.650, **POP** > 10. Molecular dynamics (MD) simulations were carried out using Desmond [Desmond Molecular Dynamics System, D.E. Shaw Research, New York, NY, USA, 2023; Maestro–Desmond Interoperability Tools, Schrödinger, New York, NY, USA, 2023] in canonical ensemble under NPT (constant number of particles, pressure, and temperature), with a constant temperature of 300 K and pressure of 1.01325 bar. Ligand-enzyme complexes were embedded in an orthorhombic box containing SPC model water molecules, and to simulate the physiological environment Na^+ and Cl^- were added to achieve a 0.15 M final salt concentration. Before starting the MD the whole molecular assemblies were passed to the default relaxing protocol, including a series of restrained minimizations and short MD runs, to gradually lower the overall energy of the system, and then simulation started with a first 200 ns equilibration stint followed by a 2000 ns trajectory for data collection, collecting hence a total of ten thousand conformations. The time step integration, calculated using the RESPA integrator, was set to 2.0 fs, and the default temperature, pressure control protocols, as well as bonded and non-bonded interactions, short-range and long-range electrostatic interactions cutoffs values were applied. The trajectories produced during the MD simulation were analysed using the Simulation Event option provided in the Desmond package The simulation was computed using an nVidia® RTX A5000 GPU within CentOS Linux environment. Drawing of the protein structures and ligands were prepared using PyMOL (https://www.pymol.org).

4.4. Kinetics of interactions with human serum albumin (HSA) by SPR study

The HSA functionalized surface on COOH V sensor chip (Pall FortèBio) was prepared by using amine coupling (EDC/NHS) and HSA (Sigma-Aldrich A3782).[41] Briefly, HSA aqueous stock solution was diluted at the final concentration of 50 μg/mL in 10 mM sodium acetate buffer (pH 5.0), and immobilization in flow cells 1 and 3 (unmodified dextran surface in flow cell 2 was used as a reference) at a final apparent level of about 5000 RU was achieved as followed: injection of EDC/NHS (freshly mixed 0.4 M EDC and 0.1 M NHS) 1:1v/v at flow 25 μL/min1 for 4 min,injection of HSA solution at flow 25 μL/min1 for 8 min; capping on unreacted activated carboxyl groups by injection of 1 M ethanolamine solution (pH 9) at flow 25 μL/min for 8 min. Functionalized surface was then treated with repeated injection of 4 M NaCl, and conditioned overnight prior to use with pH 7.4 PBS (10 mM NaH_2PO_4 and 150 mM NaCl) as running buffer. Each cycle, without regeneration necessary, for binding assay to HSA was carried out in PBS-2 % DMSO and consisted of run buffer injection (60 s), injection of analyte single concentration for 120 s (ranging from 1 to 200 μM) at a flow 20 μL/min, and dissociation phase for 150 s (flow 20 μL/min). Each interaction was performed at least in triplicate and analyzed by using QDAT software (non-linear regression analysis of 1:1 stoichiometric reversible binding model), and double referencing.

4.5. Permeability study

Pre-coated PAMPA Plate System Gentest™ used in permeability testing was provided by Corning, (Tewksbury, MA, USA, catalogue Number: 353015). The well permeable control caffeine was obtained from Sigma-Aldrich (St. Louis, MO). The plate was taken from −20 °C and warmed to room temperature for 30 min prior to perform this permeability test. 300 μl of the compound solution in PBS buffer (200 or

100 μM depending on the solubility verification) per well and 200 μl of PBS buffer per well were added to the donor plate and acceptor plate respectively. The acceptor plate was then carefully placed on top of the donor plate and then incubated for 5 h at room temperature. The assay was performed in triplicate. Following the incubation, the 150 μL from each well for both donor and acceptor plates as well as control solutions were transferred to the separate Eppendorf tubes containing the internal standard (IS) dissolved in buffer for further UPLC-MS analysis in order to determine the compound concentration in each well. The *Pe* values were calculated next using equations, which were provided in the guideline of Pre-coated PAMPA Plate System Gentest™.[32]

CRediT authorship contribution statement

Antonio Carrieri: Writing – review & editing, Writing – original draft, Supervision, Software, Project administration, Investigation, Data curation, Conceptualization. **Alexia Barbarossa:** Writing – review & editing, Investigation, Data curation. **Modesto de Candia:** Writing – review & editing, Writing – original draft, Investigation, Data curation. **Francesco Samarelli:** Investigation, Data curation. **Cosimo Damiano Altomare:** Writing – review & editing. **Kinga Czarnota-Łydka:** Writing – review & editing. **Sylwia Sudoł-Tałaj:** Data curation, Investigation. **Gniewomir Latacz:** Data curation, Investigation. **Jadwiga Handzlik:** Writing – review & editing. **Leonardo Brunetti:** Writing – review & editing, Writing – original draft, Investigation, Data curation. **Luca Piemontese:** Writing – review & editing, Writing – original draft, Investigation, Data curation. **Francesco Limongelli:** Investigation, Data curation. **Giovanni Lentini:** Writing – review & editing, Data curation. **Alessia Carocci:** Writing – review & editing, Writing – original draft, Investigation, Data curation, Conceptualization.

Declaration of competing interest

The authors declare that they have no known competing financial interests or personal relationships that could have appeared to influence the work reported in this paper.

Data availability

Data will be made available on request.

Appendix A. Supplementary data

Supplementary data to this article can be found online at https://doi.org/10.1016/j.bmc.2024.117829.

References

1. Li Petri G, Raimondi MV, Spanò V, Holl R, Barraja P, Montalbano A. Pyrrolidine in drug discovery: a versatile scaffold for novel biologically active compounds. *Top Curr Chem.* 2021;379:1–46.
2. Vitaku E, Smith DT, Njardarson JT. Analysis of the structural diversity, substitution patterns, and frequency of nitrogen heterocycles among U.S. FDA approved pharmaceuticals. *J Med Chem.* 2014;57:10257–10274.
3. Haider S, Saify ZS, Begum N, Ashraf S, Zarreen T, Saeed SG. Emerging pharmaceutical applications of piperidine, pyrrolidine and its derivatives. *World J Pharm Res.* 2014:2277–7105.
4. Huang Y, Luedtke RR, Freeman RA, Wu L, Mach RH. Synthesis and structure-activity relationships of naphthamides as dopamine D3 receptor ligands. *J Med Chem.* 2001; 44:1815–1826.
5. Stachel SJ, Steele TG, Petrocchi A, Haugabook SJ, McGaughey G, Katharine Holloway M, Allison T, Munshi S, Zuck P, Colussi D, et al. Discovery of pyrrolidine-based β-secretase inhibitors: lead advancement through conformational design for maintenance of ligand binding efficiency. *Bioorg Med Chem Lett.* 2012;22:240–244.
6. Gauthier S, Webster C, Servaes S, Morais JA, Rosa-Neto P. *World Alzheimer report 2022: life after diagnosis: navigating treatment, care and support.* London, England: Alzheimer's Disease International; 2022.
7. Jain S, Bisht A, Verma K, Negi S, Paliwal S, Sharma S. The role of fatty acid amide hydrolase enzyme inhibitors in Alzheimer's disease Cell. *Biochem Funct.* 2022;40: 106–117.
8. Misrani A, Tabassum S, Yang L. Mitochondrial dysfunction and oxidative stress in Alzheimer's disease. *Front Aging Neurosci.* 2021;13, 617588.
9. Benek O, Korabecny J, Soukup O. A perspective on multi-target drugs for Alzheimer's disease. *Trends Pharmacol Sci.* 2020;41:434–445.
10. Lovering F, Bikker J, Humblet C. Escape from flatland: increasing saturation as an approach to improving clinical success. *J Med Chem.* 2009;52:6752–6756.
11. Carocci A, Catalano A, Turi F, Lovece A, Cavalluzzi MM, Bruno C, et al. Stereoselective modulation of P-glycoprotein by chiral small molecules. *ChemMedChem.* 2016;11:93–101.
12. Carocci A, Catalano A, Lovece A, Lentini G, Duranti A, Lucini V, et al. Design, synthesis, and pharmacological effects of structurally simple ligands for MT1 and MT2 melatonin receptors. *Bioorg Med Chem.* 2010;18:6496–6511.
13. Milani G, Cavalluzzi MM, Altamura C, Santoro A, Perrone MG, Muraglia M, et al. Bioisosteric modification of To042: synthesis and evaluation of promising use-dependent inhibitors of voltage-gated sodium channels. *ChemMedChem.* 2021;16: 3588–3599.
14. Lee SH, Purgatorio R, Samarelli F, Catto M, Denora N, Morgese MG, Tucci P, Trabace L, Kim HW, Park HS, Kim, Lee, et al. Radiosynthesis and whole-body distribution in mice of a 18 F-labeled azepino[4,3- b]indole-1-one derivative with multimodal activity for the treatment of Alzheimer's disease. *Arch Pharm.* 2023: e2300491.
15. Purgatorio R, Gambacorta N, de Candia M, Catto M, et al. First-in-class isonipecotamide-based thrombin and cholinesterase dual inhibitors with potential for Alzheimer disease. *Molecules.* 2021;26:5208.
16. Samarelli F, Purgatorio R, Lopopolo G, Deruvo C, Catto M, Andresini M, Carrieri A, Nicolotti O, De Palma, Miniero, et al. Novel 6-alkyl-bridged 4-arylalkylpiperazin-1-yl derivatives of azepino[4,3-b]indol-1(2H)-one as potent BChE-selective inhibitors showing protective effects against neurodegenerative insults. *Eur J Med Chem.* 2024; 270, 116353.
17. Carocci A, Lentini G, Catalano A, Cavalluzzi MM, Bruno C, Muraglia M, et al. Chiral aryloxyalkylamines: selective 5-HT1B/1D activation and analgesic activity. *ChemMedChem.* 2010;5:696–704.
18. Purgatorio R, de Candia M, Catto M, Carrieri A, Pisani L, De Palma et al. A. Investigating 1,2,3,4,5,6-hexahydroazepino[4,3-b]indole as scaffold of butyrylcholinesterase-selective inhibitors with additional neuroprotective activities for Alzheimer's disease. *Eur J Med Chem.* 2019;177:414–424.
19. Leuci R, Brunetti L, Laghezza A, Piemontese L, Carrieri A, Pisani L, et al. A new series of aryloxyacetic acids endowed with multi-target activity towards peroxisome proliferator-activated receptors (PPARs), fatty acid amide hydrolase (FAAH), and acetylcholinesterase (AChE). *Molecules.* 2022;27:958.
20. Myllymäki MJ, Käsnänen H, Kataja AO, Lahtela-Kakkonen M, Saario SM, Poso A, et al. Chiral 3-(4,5-dihydrooxazol-2-yl)phenyl alkylcarbamates as novel FAAH inhibitors: Insight into FAAH enantioselectivity by molecular docking and interaction fields. *Eur J Med Chem.* 2009;44:4179–4191.
21. Hart T, Macias AT, Benwell K, Brooks T, D'Alessandro J, Dokurno P, et al. Fatty acid amide hydrolase inhibitors. Surprising selectivity of chiral azetidine ureas. *Bioorg Med Chem Lett.* 2009;19:4241–4244.
22. Patel JZ, Parkkari T, Laitinen T, Kaczor AA, Saario SM, Savinainen JR, et al. Chiral 1,3,4-oxadiazol-2-ones as highly selective FAAH inhibitors. *J Med Chem.* 2013;56: 8484–8496.
23. Brunetti L, Carrieri A, Piemontese L, Tortorella P, Loiodice F, Laghezza A. Beyond the canonical endocannabinoid system. A screening of PPAR ligands as FAAH inhibitors. *Int J Mol Sci.* 2020;21:7026.
24. Carocci A, Catalano A, Bruno C, Lovece A, Roselli MG, Cavalluzzi MM, et al. N-(Phenoxyalkyl) amides as MT1 and MT2 ligands: Antioxidant properties and inhibition of Ca2+/CaM-dependent kinase II. *Bioorg Med Chem.* 2013;21:847–851.
25. Gerlits O, Ho KY, Cheng X, et al. A new crystal form of human acetylcholinesterase for exploratory room-temperature crystallography studies. *Chem Biol Interact.* 2019; 309, 108698.
26. Rossi M, Freschi M, de Camargo Nascente L, Salerno A, de Melo Viana S, Teixeira FN, et al. Sustainable drug discovery of multi-target-directed ligands for Alzheimer's disease. *J Med Chem.* 2021;64:4972–4990.
27. Kazim M, Guan L, Chopra A, Sun R, Siegler MA, Lectka T, T.. Switching a HO··· π interaction to a nonconventional OH··· π hydrogen bond: a completed crystallographic puzzle. *J Org Chem.* 2020;85:9801–9807.
28. Bertolacci L, Romeo E, Veronesi M, Magotti P, Albani C, Dionisi M, et al. A binding site for nonsteroidal anti-inflammatory drugs in fatty acid amide hydrolase. *J Am Chem Soc.* 2013;135:22–25.
29. Nicolet Y, Lockridge O, Masson P, Fontecilla-Camps JC, Nachon F. Crystal structure of human butyrylcholinesterase and of its complexes with substrate and products. *J Biol Chem.* 2003;278:41141–41147.
30. Daina A, Zoete V, V.,. A boiled-egg to predict gastrointestinal absorption and brain penetration of small molecules. *ChemMedChem.* 2016;11:1117–1121.
31. Purgatorio R, de Candia M, Catto M, Rullo M, Pisani L, Denora N, et al. Evaluation of water-soluble Mannich base prodrugs of 2,3,4,5-tetrahydroazepino[4,3- b]indol-1(6 h)-one as multitarget-directed agents for Alzheimer's disease. *ChemMedChem.* 2021; 16:589–598.
32. Chen XX, Murawski A, Patel K, Crespi CL, Balimane PV. A novel design of artificial membrane for improving the PAMPA model. *Pharm Res.* 2008;25:1511–1520.
33. Muraglia M, De Bellis M, Catalano A, Carocci A, Franchini C, Carrieri A, et al. N-aryl-2,6-dimethylbenzamides, a new generation of tocainide analogues as blockers of skeletal muscle voltage-gated sodium channels. *J Med Chem.* 2014;57:2589–2600.
34. Titov AA, Purgatorio R, Obydennik AY, Listratova AV, Borisova TN, de Candia et al. M. Synthesis of isomeric 3-benzazecines decorated with endocyclic allene moiety and exocyclic conjugated double bond and evaluation of their anticholinesterase activity. *Molecules.* 2022;27:6276.

35. Purgatorio R, Gambacorta N, Samarelli F, Lopopolo G, de et al.. Assessing the role of a malonamide linker in the design of potent dual inhibitors of factor Xa and cholinesterases. *Molecules*. 2022;27:4269.
36. de Candia M, Titov AA, Viayna A, Kulikova LN, Purgatorio R, Piergiovanni B, Niso M, et al. In-vitro and in-silico studies of annelated 1,4,7,8-tetrahydroazocine ester derivatives as nanomolar selective inhibitors of human butyrylcholinesterase. *Chem Biol Interact*. 2023;386, 110741.
37. Brunetti L, Leuci R, Carrieri A, Catto M, Occhineri S, Vinci G, et al. Structure-based design of novel donepezil-like hybrids for a multi-target approach to the therapy of Alzheimer's disease. *Eur J Med Chem*. 2022;237, 114358.
38. Wang H, Joseph JA. Quantifying cellular oxidative stress by dichlorofluorescein assay using microplate reader. *Free Rad Biol Med*. 1999;27:612–616.
39. Iacopetta D, Catalano A, Ceramella J, Barbarossa A, Carocci A, Fazio A, et al. Synthesis, anticancer and antioxidant properties of new indole and pyranoindole derivatives. *Bioorg Chem*. 2020;105, 104440.
40. Carocci A, Barbarossa A, Leuci R, Carrieri A, Brunetti L, Laghezza A, et al. Novel phenothiazine/donepezil-like hybrids endowed with antioxidant activity for a multi-target approach to the therapy of Alzheimer's disease. *Antioxidants*. 2022;11:1631.
41. Rullo M, Cipolloni M, Catto M, Colliva C, Miniero DV, Latronico T, de Candia M, Benicchi T, et al. Probing fluorinated motifs onto dual AChE-MAO B inhibitors: rational design, synthesis, biological evaluation, and early-ADME studies. *J Med Chem*. 2022;65:3962–3977.